12-16-2014

Climate coupling between temperature, humidity, precipitation, and cloud cover over the Canadian prairies

Alan K. Betts
Atmospheric Research

Raymond Desjardins
Agriculture et Agroalimentaire Canada

Devon Worth
Agriculture et Agroalimentaire Canada

Brian Beckage
University of Vermont

Recommended Citation

Betts AK, Desjardins R, Worth D, Beckage B. Climate coupling between temperature, humidity, precipitation, and cloud cover over the Canadian Prairies. Journal of Geophysical Research: Atmospheres. 2014 Dec 16;119(23):13-305.

Correspondence to:
A. K. Betts,
akbetts@aol.com

Climate coupling between temperature, humidity, precipitation, and cloud cover over the Canadian Prairies

Alan K. Betts[1], Raymond Desjardins[2], Devon Worth[2], and Brian Beckage[3]

[1]Atmospheric Research, Pittsford, Vermont, USA, [2]Agriculture and Agri-Food Canada, Ottawa, Ontario, Canada, [3]Department of Plant Biology, University of Vermont, Burlington, Vermont, USA

Abstract This analysis uses over 50 years of hourly observations of temperature, relative humidity, and opaque cloud cover and daily precipitation from 11 climate stations across the Canadian Prairies to analyze the monthly, seasonal, and long-term climate coupling in the warm season. On climate time scales, temperature depends on cloud forcing, while relative humidity depends on precipitation. The monthly climate depends on both opaque cloud cover for the current month and precipitation for both the present and past 2 months in summer. Multiple linear regression shows that anomalies of opaque cloud and precipitation explain 60–80% of the variance in the diurnal temperature range, afternoon relative humidity, and lifting condensation level on monthly time scales. We analyze the internal coupling of diurnal climate observables as a further guide to evaluating models. We couple the statistics to simplified energy and water budgets for the Prairies in the growing season. The opaque cloud observations have been calibrated against the incoming shortwave and longwave fluxes. We estimate that the drydown of total water storage on the landscape damps 56% of precipitation anomalies for the growing season on large spatial scales, although this drydown increases evapotranspiration. This couples the climatological surface fluxes to four key observables: cloud forcing, precipitation, temperature, and humidity. We estimate a climatological evaporative fraction of 0.61 for the Prairies. The observational relationships of the coupled Prairie climate system across time scale will be useful for evaluating these coupled processes in models for weather and seasonal forecasting and climate simulation.

1. Introduction

One of the fundamental issues in land-atmosphere coupling and hydrometeorology is how weather and climate depend on the interplay between precipitation, soil moisture and vegetation, clouds, and net radiation (R_n). The land-surface climate in the warm season is determined by large-scale synoptic processes, as well as this local coupling between land surface (crops, natural vegetation, and soil moisture), the atmospheric boundary layer (BL), clouds, and precipitation. Soil moisture and vegetation conditions determine the partition of the surface available energy (Q^*) into the sensible (H) and latent heat (λE) fluxes, which we may write as the simplified surface energy budget

$$Q^* = (R_n - G) = H + \lambda E \qquad (1)$$

where G is the ground storage. This partition is usually represented by the evaporative fraction

$$EF = \lambda E / (R_n - G) \qquad (2a)$$

or the Bowen ratio

$$BR = H / \lambda E \qquad (2b)$$

However, R_n depends strongly on cloud cover, which in turn depends on surface evaporation, both locally and in the source regions of advected water vapor. Models with fixed vegetation show a relatively clean partition on daily time scales: soil water and temperature are linked to EF; R_n is linked to cloud radiative forcing [*Betts*, 2004, 2007, 2009], and the height of cloud base and low cloud cover are linked to soil water [*Betts*, 2004; *Betts and Viterbo*, 2005].

Many idealized models have been used to address and try to isolate specific land-atmosphere coupling pathways [e.g., *Eltahir*, 1998; *Betts*, 2000; *Betts et al.*, 2004; *Betts and Chiu*, 2010; *Pal and Eltahir*, 2001; *Findell and*

Eltahir, 2003; *Lintner et al.*, 2013] or address the controls on convection using simplified models [*Gentine et al.*, 2013a]. Observational statistics have linked precipitation to soil moisture [*Findell and Eltahir*, 1997] and surface fluxes [*Findell et al.*, 2011], and many modeling studies have addressed the role of soil water conditions in determining summer precipitation and climate [*Beljaars et al.*, 1996; *Dickinson*, 2000; *Dirmeyer*, 2000; *Koster and Suarez*, 2001; *Ferguson and Wood*, 2011; *Ferguson et al.*, 2012]. Indeed, the more challenging issues of the impact of land-surface coupling on climate can only be addressed using fully coupled global models [*Schär et al.*, 1999; *Seneviratne et al.*, 2006; *Hohenegger et al.*, 2009]. However, observations have generally not been available on climate time scales to fully quantify land-surface-climate coupling for the warm season convective BL. Specifically, regionally extensive long-term records of precipitation can be used for hydrological modeling and water balance studies, but without observations of cloud forcing, long-term observational studies of the coupled energy budget have largely been unavailable.

The Canadian Prairie data are transforming our understanding. In addition to the standard observations of hourly pressure, temperature, humidity and wind, daily precipitation and snow depth, and conventional cloud observations, the Canadian climate data contain from the early 1950s hourly observations of opaque or reflective cloud cover in tenths, made by trained observers who have followed the same protocol for 60 years [*Manual of Standard Procedures and Practices for Weather Observing and Reporting* (*MANOBS*), 2013]. These cloud observations are transformative, because they have been calibrated against multiyear shortwave and longwave radiation data [*Betts et al.*, 2013a, hereafter B13A], to quantify the shortwave cloud forcing (SWCF), net longwave flux, and R_n. Because we have for the first time the cloud radiative forcing estimates for some 600 station years of data, we are able to statistically separate the impacts of cloud cover and precipitation on the surface climate using long-term observations. As a result, these Prairie data provide a new observational basis for understanding the coupling of physical processes at the land-surface on daily, monthly, seasonal, and climate time scales. These observational relationships will be useful for evaluating the representation of these coupled processes in large-scale models, since these are our tools for weather forecasting and climate simulation.

This paper will analyze this coupling of the diurnal cycles of temperature and humidity with precipitation and cloud cover on monthly, seasonal, and climate time scales, using long-term records from 11 stations across the Canadian Prairies. It is the fourth in a series of papers. B13A analyzed the coupling between clouds and the diurnal cycle climate over the annual cycle. They showed that there is a marked difference between a warm season state with an unstable daytime convective BL, controlled by SWCF, and a cold season state with surface snow with a stable BL, controlled by longwave cloud forcing. *Betts et al.* [2013b] showed how the warm season diurnal climate has been changed by the shift in recent decades from summerfallow (where no crops were planted) to annual cropping on 20–25% of the agricultural land in Saskatchewan. This change in cropping has cooled and moistened the summer climate, with a small increase in cloud cover and precipitation in the early growing season in June. *Betts et al.* [2014] explored the sharp climate transitions with surface snow and showed the strong coupling between cold season climate and the fraction of days with snow cover. They found that snow cover acts as a climate switch. Fresh snow cover drives the transition from a warm season convective BL to a cold season stable BL in about 5 days, as a result of the large reduction in net shortwave (SW_n), and a substantial reduction in the downwelling longwave flux (LW_{dn}). As a result, the warm season convective BL, dominated by SWCF, extends throughout the year from April to October, when there is typically no surface snow.

Here we will review the warm season climate coupling between opaque clouds, precipitation, temperature, and humidity on the daily time scale, but the primary focus is monthly and longer time scales, which are clearly of importance to the understanding of both the impact of climate on agriculture and agriculture on climate. The key landscape contribution to climate in the warm season is the transpiration and evaporation of water, which depend on vegetation phenology and soil water. The climate station data have neither soil water measurements nor measurements of the surface fluxes. However, using multiple linear regression, we can show that much of the monthly variance of the surface climate, represented by temperature, humidity, and cloud base is linked to anomalies of opaque cloud cover and precipitation, which have distinct roles in the energy and water budget. Note that the data set includes all the synoptic variability for roughly 600 station years of data, but we will not attempt here to separate our climatological analysis into any synoptic regimes.

On large spatial scales and seasonal time scales, the recent decade of gridded land data from the Gravity Recovery and Climate Experiment (GRACE) will allow us to link the drydown of total water storage (TWS) [*Yang et al.*, 2011; *Cai et al.*, 2014] to precipitation anomalies during the growing season. This will permit us to

Table 1. Climate Stations: Location and Elevation

Station Name	Station No.	Station ID	Province	Latitude	Longitude	Elevation (m)
Calgary [2010]	1	3031093	Alberta	51.11	−114.02	1084
Estevan [2010]	2	4012400	Saskatchewan	49.22	−102.97	581
Lethbridge [2005]	4	3033880	Alberta	49.63	−112.80	929
Medicine Hat [2005]	5	3034480	Alberta	50.02	−110.72	717
Moose Jaw [2010]	6	4015320	Saskatchewan	50.33	−105.55	577
Prince Albert [2010]	7	4056240	Saskatchewan	53.22	−105.67	428
Red Deer [2010]	9	3025480	Alberta	52.18	−113.62	905
Regina [2008]	10	4016560	Saskatchewan	50.43	−104.67	578
Saskatoon [2009]	11	4057120	Saskatchewan	52.17	−106.72	504
Swift Current [1994]	12	4028040	Saskatchewan	50.3	−107.68	817
Winnipeg [2007]	14	5023222	Manitoba	49.82	−97.23	239

estimate seasonal evaporation on large spatial scales from a highly simplified water budget for the Canadian Prairies. Since we can estimate R_n from opaque cloud cover and surface albedo, this gives a climatological estimate of evaporative fraction (EF) in equation (2a).

Section 2 discusses the data sources, their processing, and our methodology. Section 3 presents the dependence of the daily and annual climatology on precipitation and opaque cloud cover and shows that in the long-term summer climate, air temperature (T) is coupled to cloud cover, while relative humidity (RH) is coupled to precipitation. Section 4 uses multiple linear regression to analyze the dependence of warm season T and RH on precipitation and opaque cloud on monthly time scales. Section 5 shows the corresponding regressions between climate variables on the seasonal time scale and analyses of the internal coupling between diurnal climate variables. Section 6 constructs simplified energy and water budgets to link the growing season surface fluxes to cloud forcing, precipitation, temperature, and humidity. Section 7 presents our conclusions.

2. Data and Background

2.1. Climate Station Data

We analyzed data from the 11 climate stations listed in Table 1; the stations are all at airports across the Canadian Prairies. They have hourly data, starting in 1953 for all stations, except Regina and Moose Jaw which start in 1954. The last year with complete precipitation data available, which is critical to this analysis, is listed after the station name. Most precipitation records last 53 years or longer.

For the GRACE analysis, we used the monthly archive of the second generation adjusted precipitation data set [*Mekis and Vincent*, 2011] which included additional stations shown in Table S1 in the supporting information.

2.2. Variables and Data Processing

The hourly climate variables include air pressure (p), dry bulb temperature (T), relative humidity (RH), wind speed and direction, total opaque cloud amount, and total cloud amount. Trained observers have followed the same cloud observation protocol for 60 years [*MANOBS*, 2013]. Opaque (or reflective) cloud is defined (in tenths) as cloud that obscures the Sun or the Moon and stars at night. The long-term consistency of these hourly opaque cloud fraction observations makes them useful for climate studies. B13A used four stations: Lethbridge, Swift Current, Winnipeg, and The Pas (in the boreal forest) with downward shortwave radiation SW_{dn} to calibrate the daily mean total opaque cloud fraction in terms of daily SWCF and downward longwave radiation LW_{dn} from Saskatoon and Prince Albert National Park for the calibration to net longwave (LW_n) on daily time scales.

We generated a file of daily means for all variables, such as mean temperature and humidity, T_m and RH_m, and extracted and appended to each daily record the corresponding hourly data at the times of maximum and minimum temperature (T_x and T_n). We merged a file of daily total precipitation and daily snow depth. Since occasional hourly data were missing, we kept a count of the number of measurement hours, MeasHr, of valid data in the daily mean. In our results here, we have filtered out all days for which MeasHr < 20. However, with

almost no missing hours of data in the first four decades, there are very few missing analysis days, except for Swift Current, where nighttime data are missing from June 1980 to May 1986, and Moose Jaw, where nighttime measurements ceased after 1997.

From the hourly data, we compute the diurnal temperature range between maximum temperature, T_x, and minimum temperature, T_n, as

$$DTR = T_x - T_n \tag{3}$$

We also define the difference of relative humidity, RH, between T_n and T_x, as

$$\Delta RH = RH_{tn} - RH_{tx} \approx RH_x - RH_n \tag{4}$$

where RH_x and RH_n are the maximum and minimum RH. This approximation is excellent in the warm season, when surface heating couples with a convective boundary layer (BL). Then typically, RH reaches a maximum near sunrise at T_n and a minimum at the time of the afternoon T_x [B13A]. We also derived from p, T_x, and RH_{tx} the lifting condensation level (LCL), the pressure height to the LCL, P_{LCLtx}, mixing ratio (Q_{tx}), and θ_{Etx}, all at the time of the maximum temperature.

2.3. Methodology

Our objective is to understand how precipitation and cloud cover determine the climatology of temperature and humidity on the Prairies in the warm season. We will address a range of time scales: daily, monthly, seasonal, and the 50 year long-term climate. On daily time scales, there is a strong coupling between reflective cloud cover and T_x, DTR, RH_{tx}, and ΔRH [B13A] that is similar for all the months of April to October with no snow cover. In section 3.1, we will briefly extend this analysis with the additional stratification by daily precipitation for midsummer, July, and August. While opaque cloud cover determines R_n on all time scales, precipitation controls the water balance on monthly, seasonal, and climate time scales. These will be the main focus of this paper.

We merge the data from the 11 Prairie stations in Table 1, since B13A showed a common coupling between diurnal climate and opaque cloud across the Prairies, recognizing that a more detailed analysis of individual stations may be useful later. For each variable Y, for each station, we derived from the daily data a monthly mean, Y_M, and a monthly anomaly δY, where

$$\delta Y = Y - Y_M \tag{5}$$

so the seasonal cycle is removed from the monthly anomalies. We derived a similar mean and anomaly for the May, June, July, and August (MJJA) warm season period with peak solar irradiance. For this paper we will define MJJA as the growing season. Annual crops on the Prairies are typically planted during May, while perennial crops may green up earlier, and annual crops are typically harvested by the end of August. We accepted for analysis all warm season months with >28 days of daily mean data: for MJJA, this threshold led to the rejection of only 7 months out of 2348.

3. Dependence of Climatology on Precipitation and Cloud Cover

3.1. Daily Climatology in the Warm Season

B13A showed the climatological coupling between opaque cloud and the diurnal cycles of T and RH over the annual cycle. They found a common structure in the warm season (with no surface snow cover) in which T_x decreased and RH_{tx} increased with increasing opaque cloud cover. They also showed that the diurnal ranges, DTR and ΔRH, were important, because their coupling to cloud cover was almost invariant across the Prairies.

Daily precipitation itself increases as opaque cloud and RH increase, and both are coupled to the synoptic scale forcing, but we have sufficient data to partition the dependence of the daily climate on both cloud and precipitation for each Prairie station. The seasonal cycle of temperature has a peak in July and August (see section 3.2), so we merged the daily data for July and August for the 11 stations in Table 1 and partitioned the data into three ranges of daily precipitation: <1 mm/d (largest group of 30,170 days), 1 to 4 mm/d (4760 days), and >4 mm/d (4935 days). The mean daily precipitation values for the three groups are 0.1, 2.1, and 12.4 mm. We derived the daily climatological coupling for each station and then derived a Prairie mean for the 11 stations.
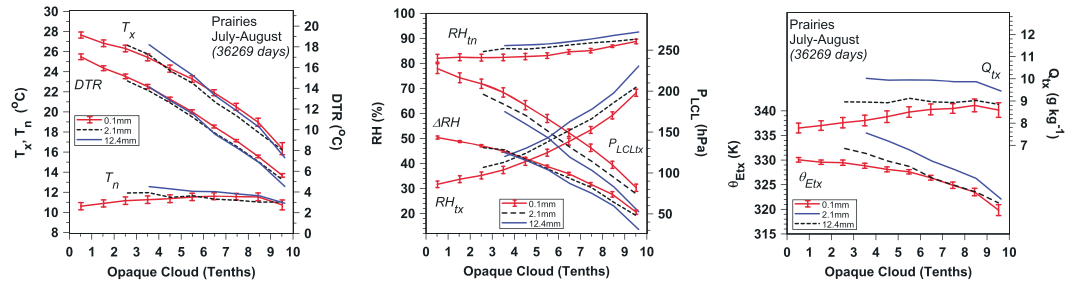
Figure 1. Mean climatology of the coupling between (left) opaque cloud, precipitation, T_x, T_n, and DTR; (middle) RH_{tn}, RH_{tx}, ΔRH, and P_{LCLtx}; and (right) θ_{Etx} and Q_{tx}.

Figure 1 (left) shows that the daily relationship between cloud, T_x, T_n, and DTR changes remarkably little with precipitation, although the days with the most rain are slightly warmer for the midrange of cloud cover. T_x and DTR decrease steeply with increasing cloud cover, while T_n barely changes [B13A]. Figure 1 (middle) shows that RH_{tx} (the afternoon minimum RH) increases with increasing cloud, while RH_{tn} (the maximum RH near sunrise) changes little, so ΔRH also decreases with cloud. However, as mean precipitation increases from 0.1 to 12.4 mm/d, the profile of RH_{tx} shifts upward by about 7%, while the pressure height of the afternoon LCL shifts downward by about 25 hPa. Figure 1 (right) shows that afternoon equivalent potential temperature, θ_{Etx}, and mixing ratio Q_{tx} both increase with precipitation.

The error bars are an estimate of the standard error on the daily time scale in the climatological coupling to opaque cloud for the 0.1 mm/d case, calculated as the standard deviation across the 11 stations divided by $\sqrt{N}$, where $N = 11$. Note that the uncertainty for DTR and ΔRH is much smaller on this daily time scale than T_x or RH_{tx}.

The variables we show characterize the surface diurnal climate and the mixed layer coupling of the subcloud boundary layer (BL) climate variables in the warm season, since the LCL is typically cloud base [B13A]. We can discuss the processes involved in this fully coupled system even though we cannot separate cause and effect. For example, the days with midrange cloud cover and high precipitation are moister with a higher afternoon θ_{Etx}; this is physically consistent with greater convective instability and higher precipitation. Over the whole range of cloud cover, it is not surprising that the days with no precipitation have a lower RH_{tx}, lower Q_{tx}, and higher LCL. However, the higher RH_{tx} and Q_{tx} for days with high precipitation can be caused by either moisture convergence or the evaporation of falling rain. Note that embedded in this fully coupled system is the full range of synoptic variability over about 600 station years of data, but this analysis will focus on the climatological coupling in the station data on different time scales and make no attempt to separate the role of the synoptic forcing.

Figure 1 can be used to assess how well the climate coupling between different surface and BL variables are represented in models on the daily time scale. It also shows that on the daily time scale, the variability of cloud cover has a larger correspondence to the variability of T_x, DTR, RH_{tx}, and P_{LCLtx} than the variability of daily precipitation. We shall see in subsequent sections that these relationships change radically on monthly, seasonal, and longer time scales. This is because, while cloud cover determines R_n on all time scales, soil water, for which we have no direct measurements, is linked to precipitation and evapotranspiration on longer time scales. *Betts et al.* [2013b] showed that in the drydown after rain events >4 mm/d, T_x falls about 2°C in the first day after rain and then recovers over 5 days, while the profile of RH_m shifts downward by about 7% over 5 days, consistent with the RH difference seen in Figure 1 between the 0.1 and 12.4 mm/d precipitation climatologies.

3.2. Annual Climatology

Figure 2 shows the annual cycle of the monthly mean climatology, stratified by anomalies of precipitation (top row) and opaque cloud cover (bottom row). The first column shows cloud and precipitation, where the data have been binned in ranges. The central dashed black line is for $-0.5 < \delta X < 0.5$, the red curve is for $-1.5 < \delta X < -0.5$, and the blue curve is $0.5 < \delta X < 1.5$, where X is the monthly precipitation in mm/d in
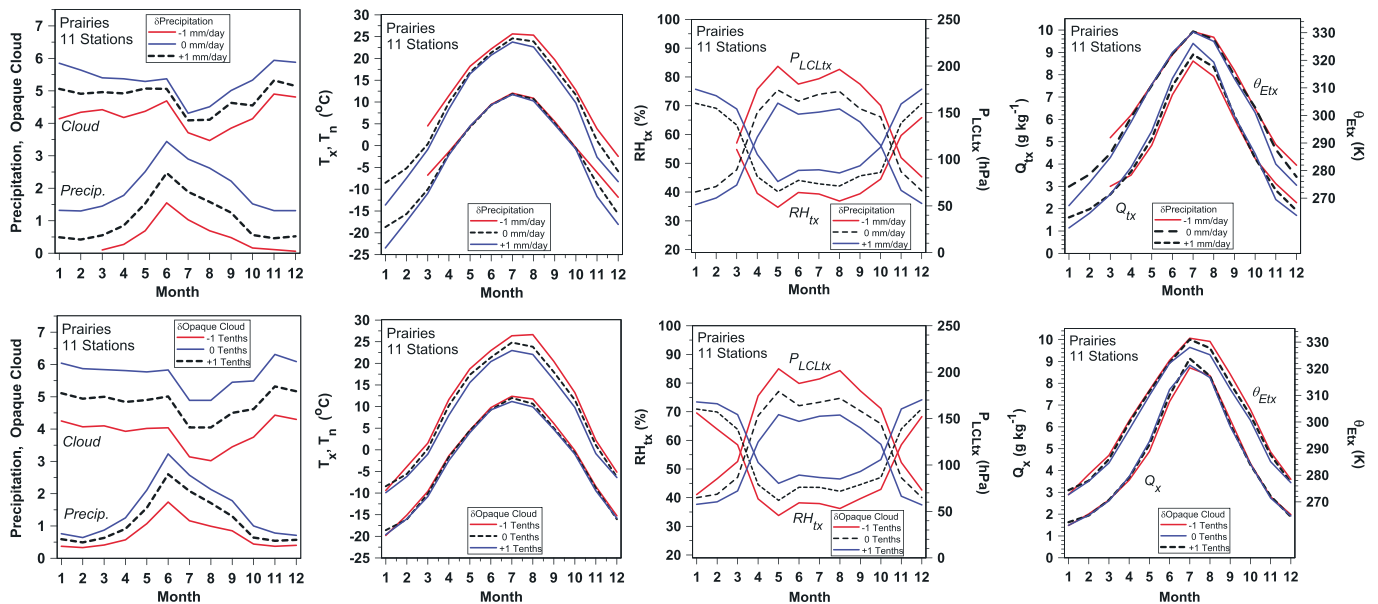
Figure 2. Annual cycle of precipitation and cloud, T_x and T_n, RH_{tx} and P_{LCLtx}, and Q_{tx} and θ_{Etx} stratified by (top row) precipitation and (bottom row) opaque cloud anomalies from station long-term means.

Figure 2 (top) and opaque cloud cover in tenths in Figure 2 (bottom). The black dashed curves are close to the mean of all the station data (not shown), and wetter or cloudier conditions are represented by the blue curves.

Precipitation is at minimum in winter, when it falls as snow, reaches a maximum in June and falls through the summer season. Opaque cloud cover peaks in June and falls sharply in July. Not surprisingly, there is more cloud in wet months than in dry months (top left), but note that if August is dry, cloud cover continues to fall to an August minimum, but if August is wet, the cloud cover minimum is in July.

The second column shows T_x and T_n, with the same stratification by precipitation and cloud anomalies. Maximum temperatures increase in all seasons from the wet to dry climatologies, with the largest increase in winter. This is because less snowfall in winter gives a warmer climatology [*Betts et al.*, 2014]. Dry conditions in summer push the seasonal maximum of T_x from July to August, presumably because the soil dries out. Minimum temperatures are insensitive to precipitation in the warm season [B13A] but fall along with T_x in winter with increasing snow. Changes in cloud cover have little effect on winter temperature, unlike changes in frozen precipitation. In summer, reduced cloud increases surface SW_{dn}, and we see that T_x increases more with 10% reduced cloud cover than with 1 mm/d reduced precipitation. The change of T_n with cloud is small.

The third column shows the climatology of RH_{tx}, P_{LCLtx} at the time of the afternoon T_x. P_{LCLtx} depends strongly on RH_{tx}, so they mirror each other. Reduced cloud cover or less precipitation is not surprisingly coupled to a lower RH and a higher LCL. The crossovers where RH_{tx} and P_{LCLtx} change sharply correspond to the mean dates of the fall-winter and winter-spring transitions that occur with snowfall and the melt of the snowpack in March and November. These mark the transitions between the warm season with an unstable convective BL and the cold season with surface snow that has a stable BL [*Betts et al.*, 2013a, 2014]. RH_{tx} is high in winter as it moves closer to saturation over ice with snow cover and reaches an afternoon low in the warm season with a deep convective BL.

The fourth column (top) shows that in summer, afternoon Q_{tx} increases with precipitation, and presumably more evaporation or more water vapor convergence, but θ_{Etx} does not, because the increase of Q_{tx} is offset by the decrease of T_x. In winter, Q_{tx} decreases with more snow and colder temperatures. Figure 2 (lower right) shows that while Q_{tx} does not change systematically with cloud cover, θ_{Etx} does increase with less cloud cover because of the increase of T_x.
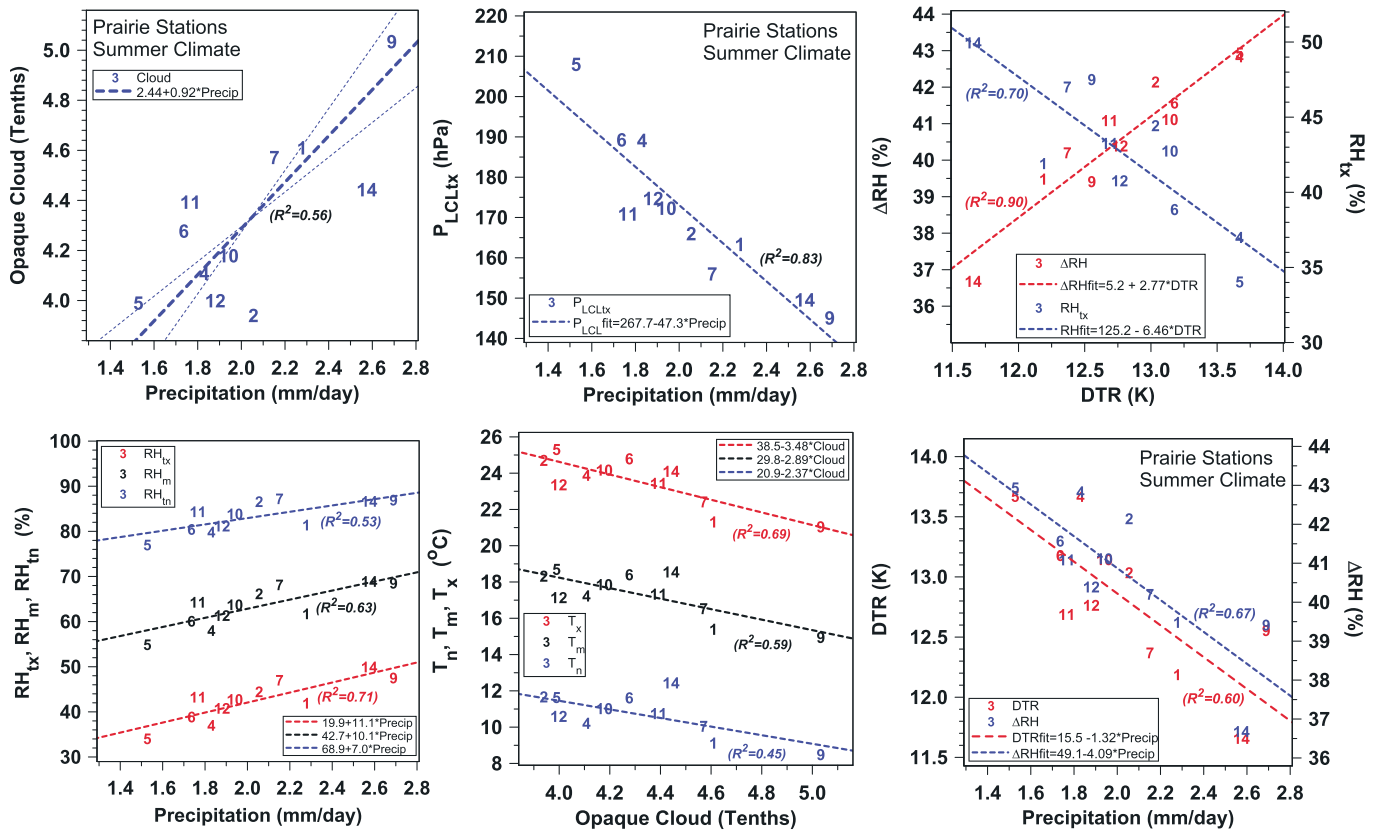
Figure 3. Spatial relationships between (top left) opaque cloud and precipitation; (top middle) P_{LCLtx} and precipitation; and (top right) ΔRH, RH_{tx}, and DTR. (bottom left) RH_{tx}, RH_m, RH_{tn}, and precipitation; (bottom middle) T_x, T_m, T_n, and opaque cloud; and (bottom right) DTR and ΔRH and precipitation for the station long-term summer means.

The differences in Figure 2 between changes of precipitation and changes of cloud seem relatively small, but cloud and precipitation are not tightly coupled on monthly time scales. As a result, if we are to understand growing season climate, we must account for both changes in precipitation that impact soil water and evaporation, as well as cloud cover that affect net radiation.

3.3. Long-Term Summer Climate Across the Prairies

From the reduced daily data sets, we constructed long-term monthly climate means for each station for the months of April to October for the following variables: precipitation, opaque cloud, T_x, T_m, T_n, DTR, RH_{tx}, RH_m, RH_{tn}, ΔRH, Q_{tx}, P_{LCLtx}, and θ_{Etx}. From these monthly means, we then generated a mean climatology for the warmest summer months (June, July, and August), including only those years where all 3 months had more than 28 days of good data. The average station record length is 53 years.

Figure 3 (top left) shows the relationship between opaque cloud and precipitation, with the linear regression fits ($R^2 = 0.56$) of cloud on precipitation and precipitation on cloud (dotted lines) and the geometric mean (dashed line), with slope of 0.92 ± 0.27, where this poorly known uncertainty estimate is simply half the difference of the slopes of the dotted lines.

The points are identified by their station numbers in Table 1. The mean opaque cloud cover increases with increasing mean precipitation. This reflects the association of precipitation with clouds, and the fact that some but not all of the cloud cover is coupled to local evapotranspiration, which in the long-term mean is linked on precipitation. Figure 3 (top middle) shows the much tighter coupling of afternoon $P_{LCLtx} = (47.3 \pm 7.2)$ to precipitation ($R^2 = 0.83$). We interpret this as precipitation determines summer soil moisture, and soil moisture determines the surface vegetative resistance to transpiration, which largely controls the vapor pressure deficit near the surface, as well as the LCL, mixed layer

depth, and sensible heat flux [*Betts*, 2000; *Betts et al.*, 2004; *Betts*, 2009; *Betts and Chiu*, 2010]. These links are well documented in models [*Betts*, 2004; *Betts and Viterbo*, 2005; *Ferguson et al.*, 2012], but these data suggest that they are observed as warm season climate characteristics for the Prairies. Figure 3 (top right) shows the regression on the diurnal temperature range, giving $\Delta RH = (2.77 \pm 0.32)$ DTR ($R^2 = 0.90$) and $RH_{tx} = (-6.46 \pm 1.40)$ DTR ($R^2 = 0.70$). We will revisit these internal coupled characteristics of the warm season BL in section 5.2 with monthly and seasonal data sets.

Figure 3 (bottom left) shows that the moisture variables, RH_{tx}, RH_m, and RH_{tn}, all increase with precipitation. The regression slopes of RH_{tx}, RH_m, and RH_{tn} on precipitation have decreasing values (11.1 ± 2.4, 10.1 ± 2.6, and 7.0 ± 2.2%/mm/d), and the corresponding linear regression R^2 values (0.71, 0.63, and 0.53) also decrease. Figure 3 (bottom middle) is a similar plot for T_x, T_m, and T_n, but the x axis is now opaque cloud. Air temperature decreases with increasing cloud cover. The regression slopes of T_x, T_m, and T_n with opaque cloud have decreasing values (3.48 ± 0.78, 2.89 ± 0.82, and 2.37 ± 0.88°C/10% cloud), and the corresponding linear regression R^2 values are 0.69, 0.59, and 0.45. Figure 3 (bottom right) presents DTR and ΔRH against precipitation, showing that both decrease as precipitation increases. The regression slopes are -1.32 ± 0.36°C/mm/d for DTR ($R^2 = 0.60$) and 4.09 ± 0.97%/mm/d for ΔRH ($R^2 = 0.67$). The near overlap of many pairs of points reflects the very tight coupling of DTR and ΔRH shown above. For the corresponding plot of DTR and ΔRH against opaque cloud, the linear regression fits are much weaker with $R^2 = 0.36$ for both (not shown).

The multiple linear regression of RH variables and DTR on precipitation and cloud shows that precipitation explains almost all the variance in the spatial relationship of the long-term station climate means. For example,

$$RH_x = 22.9(\pm 2.8) + 11.8(\pm 3.8)*Precip - 1.0(\pm 4.1)*OpaqueCloud \ (R^2 = 0.71)$$

Similarly, the multiple linear regression of T_x, T_m, and T_n on precipitation and opaque cloud shows that opaque cloud explains almost all the variance. For example,

$$T_x = 38.0(\pm 0.9) - 0.39(\pm 1.15)*Precip - 3.2(\pm 1.2)*OpaqueCloud \ (R^2 = 0.69)$$

We interpret this remarkable simplification (which we shall see is not true on monthly and seasonal time scales) as meaning that on this 50 year climate time scale, mean air temperatures are determined by opaque cloud cover, because this determines daily net radiation [B13A]. However, precipitation determines RH and P_{LCLtx} through the impact of soil moisture on the stomatal control of subsaturation [*Betts*, 2004; *Betts et al.*, 2004]. The diurnal ranges of temperature and RH, which are very tightly coupled, are also determined by the variability of precipitation, presumably because soil moisture and stomatal control determine EF and the partition of the net radiation.

The relationship of temperature and RH changes across time scale. They are anticorrelated on the diurnal time scale, but on climate time scales in our spatial analysis, we see that they are coupled to different processes: temperature to R_n and RH to precipitation. This is of profound significance in meteorology, although it is not widely appreciated, perhaps because many traditional texts downplay the significance of RH as a fundamental variable. Mixing ratio, Q, which is important as a conserved quantity in the absence of atmospheric condensation/evaporation processes, is defined as

$$Q = \varepsilon e/(p - e) \approx \varepsilon e/p = \varepsilon RH\, e_s(T)/p \tag{6}$$

where $\varepsilon = 0.622$, p is the atmospheric pressure, e is the vapor pressure, and $e_s(T)$ is the saturation vapor pressure. Hence, Q is a product of RH and $e_s(T)$ which is a function only of T. In the long-term summer climate of these 11 Prairie stations, Q has very small correlation with precipitation ($R^2 = 0.25$), and no correlation with opaque cloud ($R^2 = 0.00$), but the multiple regression on both has a much higher correlation with $R^2 = 0.50$.

$$Q = 10.9(\pm 0.6) + 2.1(\pm 0.7)*Precip - 1.6(\pm 0.8)*OpaqueCloud \tag{7a}$$

Similarly, θ_E, which also depends on temperature and RH, has no correlation with precipitation ($R^2 = 0.00$), and only a small correlation with opaque cloud ($R^2 = 0.28$), but the multiple regression on both has a much higher correlation with $R^2 = 0.54$.

$$\theta_E = 343.2(\pm 1.2) + 3.5(\pm 1.6)*Precip - 5.5(\pm 1.8)*OpaqueCloud \tag{7b}$$

BETTS ET AL. 13,312

Table 2. Regression Coefficients for Months of May to October for δT_x, δDTR, δRH$_{tx}$, and δP_{LCLtx}[a]

Month δT_x	K	A	B	C	D	R^2 (8)	R^2 δPrecipWT	R^2 δCloud	σ (δY)
May	0 ± 1.5	(-0.10 ± 0.16)	-0.52 ± 0.10	0.02 ± 0.07	-1.69 ± 0.09	0.49	0.18	0.47	2.12
Jun	0 ± 1.3	(-0.16 ± 0.08)	-0.28 ± 0.06	0.00 ± 0.04	-1.67 ± 0.08	0.49	0.10	0.46	1.82
Jul	0 ± 1.1	(-0.09 ± 0.05)	-0.19 ± 0.03	-0.29 ± 0.05	-1.68 ± 0.08	0.58	0.27	0.52	1.74
Aug	0 ± 1.4	(0.02 ± 0.04)	-0.26 ± 0.05	-0.34 ± 0.06	-1.83 ± 0.08	0.66	0.33	0.62	2.39
Sept	0 ± 1.4	(-0.07 ± 0.05)	-0.18 ± 0.05	-0.22 ± 0.07	-2.07 ± 0.06	0.74	0.26	0.73	2.66
Oct	0 ± 1.6	(-0.09 ± 0.06)	-0.20 ± 0.07	-0.26 ± 0.15	-2.00 ± 0.09	0.58	0.18	0.57	2.48
δDTR	-	-	-	-	-	-	-	-	-
May	0 ± 0.77	(-0.08 ± 0.08)	-0.37 ± 0.05	-0.37 ± 0.04	-1.16 ± 0.05	0.73	0.41	0.66	1.46
Jun	0 ± 0.70	(-0.11 ± 0.04)	-0.30 ± 0.03	-0.32 ± 0.02	-0.97 ± 0.04	0.69	0.42	0.52	1.25
Jul	0 ± 0.73	-0.20 ± 0.03	-0.25 ± 0.02	-0.33 ± 0.03	-1.10 ± 0.05	0.67	0.42	0.48	1.25
Aug	0 ± 0.74	-0.07 ± 0.02	-0.21 ± 0.03	-0.40 ± 0.03	-1.24 ± 0.04	0.79	0.46	0.71	1.63
Sept	0 ± 0.77	(-0.04 ± 0.03)	-0.22 ± 0.03	-0.49 ± 0.04	-1.27 ± 0.04	0.82	0.43	0.75	1.81
Oct	0 ± 0.78	(-0.09 ± 0.03)	-0.27 ± 0.03	-0.70 ± 0.07	-1.33 ± 0.04	0.77	0.37	0.70	1.64
δRH$_{tx}$	-	-	-	-	-	-	-	-	-
May	0 ± 3.5	1.30 ± 0.37	1.47 ± 0.22	2.07 ± 0.17	4.75 ± 0.20	0.72	0.46	0.62	6.53
Jun	0 ± 3.6	0.69 ± 0.23	1.26 ± 0.15	1.96 ± 0.12	4.36 ± 0.22	0.68	0.47	0.48	6.37
Jul	0 ± 4.1	0.84 ± 0.18	1.71 ± 0.12	1.81 ± 0.17	4.40 ± 0.30	0.59	0.43	0.32	6.35
Aug	0 ± 3.6	0.65 ± 0.11	1.23 ± 0.13	2.43 ± 0.16	4.07 ± 0.20	0.73	0.53	0.56	6.93
Sept	0 ± 3.5	(0.22 ± 0.12)	1.40 ± 0.13	2.10 ± 0.18	4.35 ± 0.16	0.75	0.45	0.63	7.01
Oct	0 ± 4.3	(0.33 ± 0.16)	1.28 ± 0.19	5.02 ± 0.39	4.58 ± 0.23	0.67	0.44	0.53	7.44
δP_{LCLtx}	-	-	-	-	-	-	-	-	-
May	2 ± 15	-4.8 ± 1.6	-6.6 ± 1.0	-8.6 ± 0.7	-21.6 ± 0.9	0.73	0.45	0.64	28.7
Jun	2 ± 15	-2.9 ± 0.9	-5.2 ± 0.6	-7.7 ± 0.5	-19.1 ± 0.9	0.69	0.45	0.51	26.4
Jul	2 ± 17	-3.8 ± 0.7	-7.4 ± 0.5	-7.5 ± 0.7	-19.4 ± 1.2	0.60	0.43	0.33	27.1
Aug	2 ± 16	-2.9 ± 0.5	-5.4 ± 0.6	-9.6 ± 0.7	-18.7 ± 0.9	0.72	0.50	0.57	30.3
Sept	2 ± 14	(-1.0 ± 0.5)	-5.5 ± 0.5	-8.0 ± 0.7	-18.3 ± 0.6	0.76	0.44	0.65	28.5
Oct	2 ± 16	(-1.1 ± 0.6)	-4.6 ± 0.7	-17.2 ± 1.4	-16.9 ± 0.8	0.66	0.42	0.53	27.0

[a]The column of R^2 (equation (8)) uses all the terms in equations (8) or (10); $R^2(\delta$PrecipWT) is the regression on just the precipitation term in equation (10), and $R^2(\delta$Cloud) is for the regression on just the opaque cloud term.

4. Coupling of Climate Variables in the Warm Season

Section 3.1 showed how the daily climate is dominated by the variability of opaque cloud cover in midsummer. Section 3.3 looked at the coupling of the long-term summer climate to precipitation and opaque cloud across the 11 Prairie stations. On climate time scales, precipitation controls the water balance, resulting in a tight coupling of the moisture variables and DTR to precipitation. Opaque cloud cover determines net radiation [B13A], giving a tight coupling of the temperature variables (but not DTR) to opaque cloud. This section will show how these relationships are different on monthly and seasonal time scales.

4.1. Regression Analysis of Monthly Mean Anomalies

For each station and each month, we removed the station monthly means (equation (5)) and then merged the station anomalies. This gives about 585 station years of data for each month. We calculated the regression fits for the warm season months of May to October, for $Y = T_x$, DTR, RH$_x$, P_{LCL}, and other variables in the form

$$\delta Y = K + A * \delta\text{Precip(Mo-2)} + B * \delta\text{Precip(Mo-1)} + C * \delta\text{Precip} + D * \delta\text{OpaqueCloud} \qquad (8)$$

Equation (8) includes precipitation anomalies for two previous months, but opaque cloud anomalies only for the current month, because previous months make no contribution to the explained variance. Table 2 shows the regression coefficients for equation (8) for δT_x, δDTR, δRH$_{tx}$, and δP_{LCLtx}. The standard deviations of monthly precipitation anomalies for the 7 months of April, May, June, July, August, September, and October (AMJJASO) are 0.66, 0.98, 1.40, 1.18, 1.14, 0.95, and 0.54 mm/d, and for the opaque cloud anomalies for MJJASO, they are 0.85, 0.76, 0.67, 0.93, 1.04, and 0.92. The three precipitation terms, representing the memory of the current climate to current and past precipitation, can also be collapsed into one by defining a weighted precipitation using the three regression coefficients

$$\delta\text{PrecipWT} = A_n * \delta\text{Precip(Mo-2)} + B_n * \delta\text{Precip(Mo-1)} + C_n * \delta\text{Precip} \qquad (9)$$
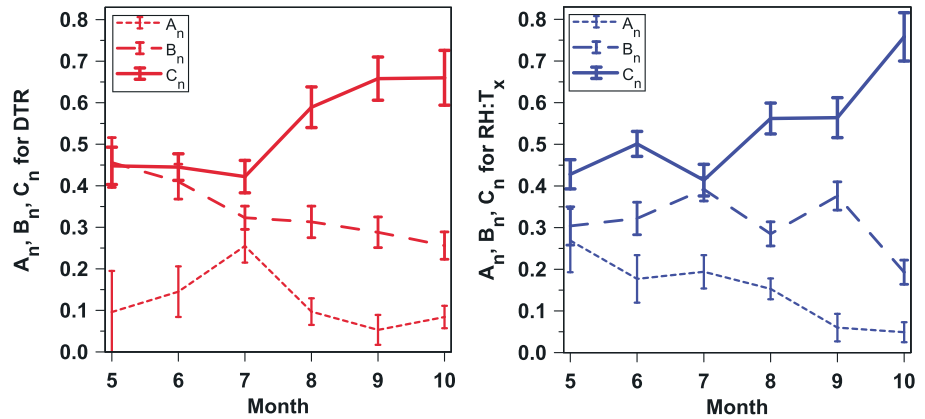
Figure 4. Seasonal cycle of scaled precipitation weights for (left) DTR and (right) RH_{tx}, where $A_n = A/(A + B + C)$.

where the weights have been scaled by their sum: $A_n = A/(A + B + C)$. Then the regression simplifies, with the same R^2 coefficient, to

$$\delta Y = K + (A + B + C)^* \, \delta PrecipWT + D^* \, \delta OpaqueCloud \qquad (10)$$

The last column in Table 2, $\sigma(\delta Y)$, is the standard deviation of δY. Note that the ratio of these standard deviations is the best estimate of the internal relationship between variables: for example, the slope of RH_{tx} on DTR for September = 7.01/1.81 = 3.87%/°C (see Table 5 later).

The explained variance is as high as 0.82 for DTR and 0.75 for RH_{tx} in September but considerably lower in July at peak crop growth. The values in the parenthesis contribute very little to the explained variance. There are many months when the contribution of $\delta Precip(Mo-2)$ is insignificant. The R^2 values in the last two columns give an indication of the relative importance of precipitation and cloud anomalies for a given variable and month. Opaque cloud anomalies are the dominant contribution for T_x and DTR. For RH_{tx} and P_{LCLtx}, the contribution from precipitation anomalies is comparable to that of opaque cloud for JJA and dominant in July at peak crop growth. It is clear that both opaque cloud (which determine R_n—see section 6.4) and precipitation play crucial roles in determining the monthly climatology of land-surface coupling in the warm season.

Note that the climate memory is not in the precipitation anomalies themselves. The 1 month lagged autocorrelation of precipitation anomalies, $\delta Precip$ on the preceding month $\delta Precip(Mo-1)$, for the 2341 growing season months (MJJA) has $R^2 = 0.000$; so precipitation anomalies, $\delta Precip(Mo-2)$ and $\delta Precip(Mo-1)$, $\delta Precip$ can be treated as independent. Models show that the memory is in soil moisture [*Koster and Suarez*, 2001; *Beljaars et al.*, 1996; *Betts*, 2004].

4.2. Seasonal Cycle of Scaled Precipitation Regression Weights

Figure 4 shows the relative importance over the seasonal cycle of the scaled precipitation weights A_n, B_n, and C_n for DTR and RH_{tx}, defined in equation (9). The error estimates are derived from Table 2. The coefficients for P_{LCLtx} are similar to RH_{tx} (not shown), and T_x has less dependence on precipitation (Table 2). The influence of C_n, representing correlation of precipitation variability to climate for the current month, is generally larger than B_n, representing the previous month. B_n is an important term in May, June, and July, but by October, $C_n >> B_n$. The lagged memory of $\delta Precip(Mo-2)$, represented by A_n, is smallest; it explains little of the variance in the multiple regression in May and June, when the standard deviation is large, and in September and October, when A_n is small. Interestingly, the contribution of A_n for DTR peaks in July, indicating that deeper crop rooting at the peak of the growing season can perhaps access soil water from deeper layers stored from the spring. However, July is also the month when the explained variance is the smallest (Table 2), suggesting that crop biophysical processes may play an important role. One other aspect that has been left for future work is the role of snowmelt, typically in late March, on the spring climate.
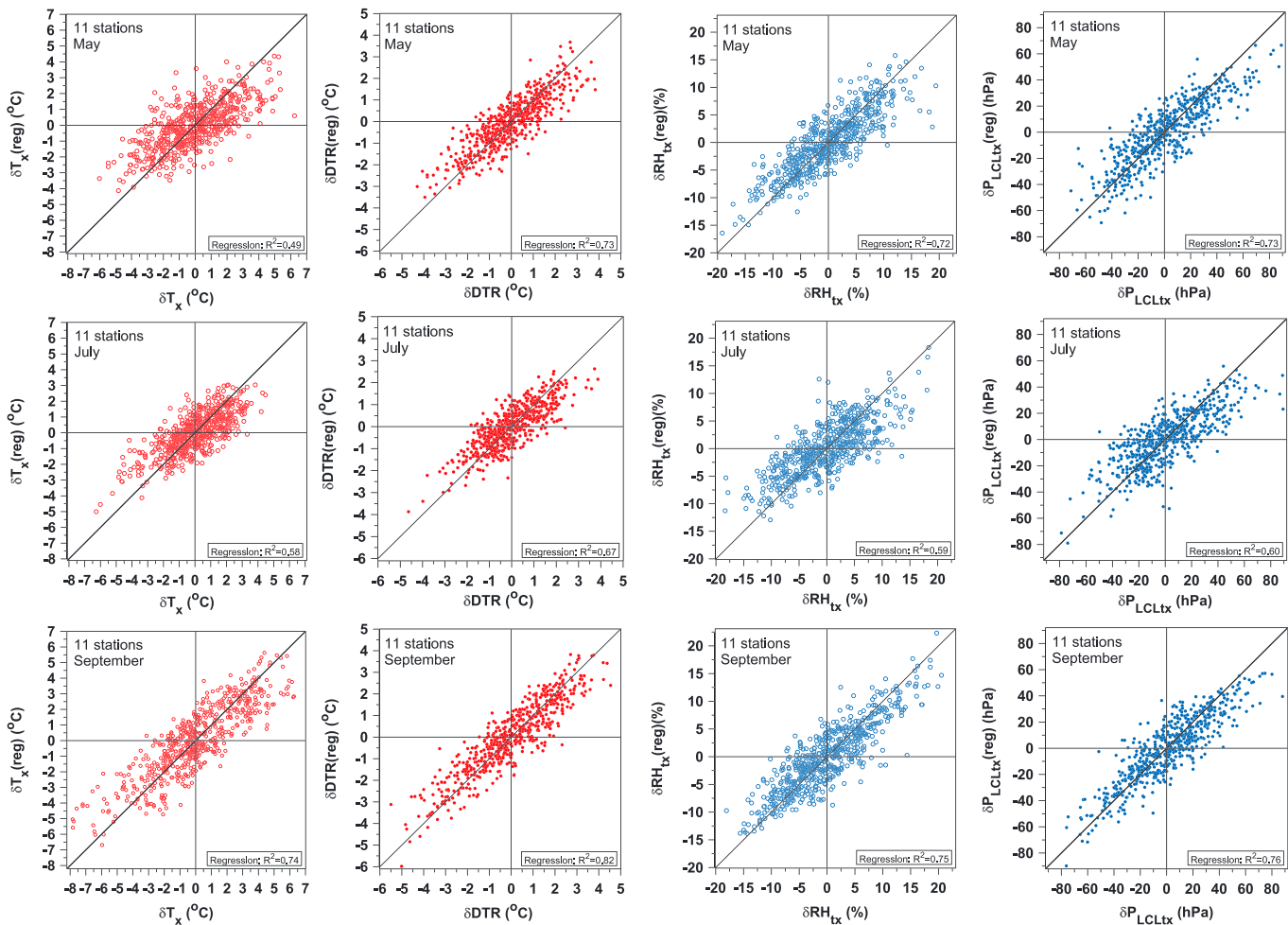
Figure 5. Regression fits from Table 2 for δT_x, δDTR, δRH_{tx}, and δP_{LCLtx} for May, July, and September.

4.3. Regression Fits for Selected Months

Figure 5 shows the scatterplots of the regression fits, δY(reg) against δY, for three representative months: May, July, and September for δT_x, δDTR, δRH_{tx}, and δP_{LCLtx} using the coefficients in Table 2 to compute δY(reg). There are about 585 months of complete data. September has both a wider range of variability and higher R^2 values than July. For T_x, we removed the regression A values on δPrecip(Mo-2), which are all insignificant. The multiple linear regression on opaque cloud and precipitation anomalies tends to underestimate anomalies at the extremes.

This may be the nonlinear vegetation response to dry and wet conditions. Nonetheless, for May to October, the regression on opaque cloud and precipitation anomalies gives (δT_x, δDTR, δRH_{tx}, and δP_{LCLtx}) with an accuracy of about ±1.4 K, ±0.75 K, ±3.8%, and ±15.5 hPa. Note that since we are compositing 50 years of data, any climate change signal is part of the noise in the analysis.

4.4. Regression Analysis Using Monthly Mean Data for the Growing Season

It is apparent from Table 2 that monthly regression coefficients are similar for the MJJA growing season, so we combined the monthly anomalies for MJJA, giving a total of 2341 months of station data. Then we calculated a single set of the regression coefficients for equation (8) that are shown in Table 3 for the full set of variables. The coefficients are similar, within their standard deviations, if just the summer months, June, July, and August, are combined. We have enclosed in parentheses values where the root-mean-square error is comparable to the mean, since these make a negligible contribution to the explained variance. Note that the R^2 (equation (8)) values are >0.55 for the five variables: T_x, DTR, RH_{tx}, RH_m, and P_{LCLtx}. Again, the R^2 values in

Table 3. Regression Coefficients for (Equation (8)) for Combined Monthly Means: May, June, July, and August

δY	K	A	B	C	D	R^2 (Equation (8))	R^2 δPrecipWT	R^2 δCloud	σ (δY)
δT_x	0 ± 1.4	(-0.04 ± 0.03)	-0.26 ± 0.03	-0.14 ± 0.03	-1.77 ± 0.04	0.55	0.19	0.52	2.03
δT_m	0 ± 1.3	(-0.01 ± 0.03)	-0.15 ± 0.02	(0.0 ± 0.03)	-1.27 ± 0.04	0.40	0.10	0.39	1.61
δT_n	0 ± 1.3	(0.06 ± 0.03)	(0.0 ± 0.03)	0.21 ± 0.03	-0.62 ± 0.04	0.10	0.0	0.08	1.36
δDTR	0 ± 0.75	-0.10 ± 0.02	-0.26 ± 0.01	-0.34 ± 0.01	-1.15 ± 0.02	0.72	0.40	0.61	1.41
δRH$_{tx}$	0 ± 3.7	0.73 ± 0.08	1.47 ± 0.07	2.03 ± 0.07	4.44 ± 0.11	0.68	0.46	0.50	6.55
δRH$_m$	0 ± 4.1	0.84 ± 0.09	1.49 ± 0.08	1.86 ± 0.08	4.22 ± 0.12	0.61	0.41	0.44	6.56
δRH$_{tn}$	0 ± 4.8	0.76 ± 0.11	1.22 ± 0.09	1.22 ± 0.10	2.82 ± 0.14	0.35	0.24	0.24	5.93
$\delta\Delta$RH	0 ± 3.8	(0.03 ± 0.08)	-0.25 ± 0.07	-0.81 ± 0.08	-1.61 ± 0.11	0.21	0.14	0.16	4.30
δP_{LCLtx}	1.7 ± 15.9	-3.23 ± 0.35	-6.37 ± 0.30	-8.11 ± 0.32	-20.0 ± 0.47	0.68	0.44	0.52	28.2
δQ_{tx}	-0 ± 0.8	0.14 ± 0.02	0.17 ± 0.01	0.29 ± 0.02	(0.0 ± 0.02)	0.23	0.23	0.03	0.87
$\delta \theta_{Etx}$	-0.2 ± 3.2	0.37 ± 0.07	0.23 ± 0.06	0.69 ± 0.06	-1.95 ± 0.10	0.17	0.02	0.11	3.53

the last two columns indicate the relative importance of precipitation and cloud anomalies. The precipitation anomalies make very little contribution to the explained variance of T_x, and the opaque cloud anomalies make no contribution to the small explained variance of Q. Most variables are correlated with opaque cloud anomalies, as seen on the daily time scale [B13A]. However, the precipitation variables play a significant role in the DTR and moisture anomalies, as seen in Table 2 for the separate months. The last column is again the standard deviation for each variable.

The regression fits given by equation (10) give the slopes with unit changes of δPrecipWT in mm/d and δOpaqueCloud in tenths.

$$\delta T_x = -0.44(\pm 0.04)\delta\text{PrecipWT} - 1.77(\pm 0.04)\delta\text{OpaqueCloud} \quad (R^2 = 0.55) \tag{11a}$$

$$\delta\text{DTR} = -0.71(\pm 0.02)\delta\text{PrecipWT} - 1.15(\pm 0.02)\delta\text{OpaqueCloud} \quad (R^2 = 0.72) \tag{11b}$$

$$\delta\text{RH}_{tx} = 4.19(\pm 0.12)\delta\text{PrecipWT} + 4.45(\pm 0.10)\delta\text{OpaqueCloud} \quad (R^2 = 0.68) \tag{11c}$$

$$\delta P_{LCLtx} = -17.4(\pm 0.5)\delta\text{PrecipWT} - 19.8(\pm 0.4)\,\delta\text{OpaqueCloud} \quad (R^2 = 0.68) \tag{11d}$$

These combined dependencies on precipitation and opaque cloud anomalies on the seasonal time scale stand in contrast to the 50 year climate relations for summer, shown in Figure 3. For T_x, the spatial climate relation across the 11 stations showed dependence only on opaque cloud with a slope of $-3.48°C$ per tenth, whereas equation (11a), which is both a spatial and temporal relationship, shows only half that slope of $-1.77°C$ per tenth and a small precipitation dependence of $-0.44°C$/mm/d. Similarly, the Figure 3 climate relation for RH$_{tx}$ depended only on precipitation with a slope of 11.1%/mm/d, whereas equation (11c) shows a precipitation dependency of 4.19%/mm/d and an opaque cloud dependency of 4.45% per tenth. Dividing the variables by their standard deviations, given in Table 3, together with $\sigma(\delta\text{PrecipWT}, \delta\text{OpaqueCloud}) = (0.72 \text{ mm/d}, 0.80 \text{ tenths})$ gives the standardized regressions (suffix σ), with the same R^2 as equation (11).

$$\delta T_{x\sigma} = -0.15(\pm 0.01)\,\delta\text{PrecipWT}_\sigma - 0.69(\pm 0.01)\,\delta\text{OpaqueCloud}_\sigma \tag{12a}$$

$$\delta\text{DTR}_\sigma = -0.36(\pm 0.01)\,\delta\text{PrecipWT}_\sigma - 0.65(\pm 0.01)\,\delta\text{OpaqueCloud}_\sigma \tag{12b}$$

Table 4. Regression of Growing Season Standardized Climate Anomalies on Precipitation and Opaque Cloud Standardized Anomalies

Variable: δY_σ	K_σ	B_σ	C_σ	R^2(Equation (14))	σ (δY)
$\delta T_{x\sigma}$	0 ± 0.7	-0.33 ± 0.03	-0.52 ± 0.03	0.52	1.11
$\delta T_{m\sigma}$	0 ± 0.8	-0.21 ± 0.05	-0.50 ± 0.07	0.38	0.88
$\delta T_{n\sigma}$	0 ± 1.0	0.11 ± 0.04	-0.33 ± 0.04	0.09	0.77
δDTR_σ	0 ± 0.6	-0.55 ± 0.03	-0.39 ± 0.03	0.62	0.83
$\delta\text{RH}_{tx\sigma}$	0 ± 0.6	0.56 ± 0.03	0.35 ± 0.03	0.60	4.35
$\delta\text{RH}_{m\sigma}$	0 ± 0.7	0.51 ± 0.03	0.33 ± 0.03	0.50	4.61
$\delta\text{RH}_{tn\sigma}$	0 ± 0.9	0.38 ± 0.04	0.24 ± 0.04	0.27	4.52
$\delta\Delta\text{RH}_\sigma$	0 ± 1.0	-0.24 ± 0.04	-0.15 ± 0.04	0.11	2.97
$\delta P_{LCLtx\sigma}$	0 ± 0.6	-0.56 ± 0.03	-0.37 ± 0.03	0.61	18.6
$\delta Q_{tx\sigma}$	0 ± 0.9	0.50 ± 0.04	0.03 ± 0.04	0.26	0.58
$\delta \theta_{Etx\sigma}$	0 ± 1.0	0.22 ± 0.04	-0.31 ± 0.04	0.09	1.95

Table 5. Regression Coefficients for δCloud on δPrecip and δT_x, δRH$_{tx}$, $\delta\Delta$RH, and P_{LCLtx} on DTR for the Growing Season

		MJJA Mean (580 years)		May, Jun, Jul, and Aug (2341 Months)		
	$\sigma(\delta Y)$	Slope	R^2	$\sigma(\delta Y)$	Slope	R^2
δPrecip	0.597			1.185		
δCloud (on δPrecip)	0.434	0.73 ± 0.12	0.17	0.800	0.68 ± 0.07	0.24
δDTR	0.826			1.409		
δT_x (on δDTR)	1.108	1.34 ± 0.13	0.51	2.034	1.44 ± 0.05	0.56
δRH$_{tx}$ (on δDTR)	4.345	-5.26 ± 0.46	0.51	6.547	-4.65 ± 0.14	0.67
$\delta\Delta$RH (on δDTR)	2.969	3.60 ± 0.72	0.22	4.304	3.05 ± 0.20	0.30
δP_{LCLtx} (on δDTR)	18.60	22.5 ± 1.8	0.53	28.17	20.0 ± 0.6	0.69

$$\delta\text{RH}_{tx\sigma} = 0.46(\pm 0.01)\,\delta\text{PrecipWT}_\sigma + 0.54(\pm 0.01)\,\delta\text{OpaqueCloud}_\sigma \qquad (12c)$$

$$\delta P_{LCLtx\sigma} = -0.44(\pm 0.01)\,\delta\text{PrecipWT}_\sigma - 0.56(\pm 0.01)\,\delta\text{OpaqueCloud}_\sigma \qquad (12d)$$

In this form, we can see the reduction of the dependence on δOpaqueCloud$_\sigma$ and increased dependence on δPrecipWT$_\sigma$ from δT_x to δDTR to δRH$_{tx}$.

5. Growing Season Climate

In this section we move from using monthly means and their anomalies to growing season means (MJJA) and their anomalies.

5.1. Coupling of Growing Season Anomalies to Precipitation and Opaque Cloud Anomalies

We generated averages for the growing season (MJJA). There are 580 years with complete MJJA data from the 11 Prairie stations. For each station, we then removed the station means using equation (5) and looked at the multiple regression of temperature and humidity anomalies on MJJA opaque cloud and precipitation anomalies. Since we are averaging 4 months, the dependence on precipitation for the previous months are now included except for April precipitation anomalies. We checked that including April precipitation anomalies did increase the R^2 regression coefficients slightly, and we found that this improvement could be included with good precision by simply defining

$$\delta\text{Precip(AMJJA)} = 0.25 * \delta\text{Precip(April)} + \delta\text{Precip(MJJA)} \qquad (13)$$

The weighting factor of 0.25 on δPrecip (April) (in units of mm/d) comes from the reduced impact of a single month on the 4 month mean. We then divided all variables by their standard deviation to give standardized regression coefficients, shown in Table 4, for the relationship

$$\delta Y_\sigma = K_\sigma + B_\sigma * \delta\text{Precip(AMJJA)}_\sigma + C_\sigma * \delta\text{OpaqueCloud}_\sigma \qquad (14)$$

The standard deviations are 0.614 mm/d for δPrecip(AMJJA) and 0.434 tenths for δOpaqueCloud; for δY, they are shown in the right column of Table 4.

In this form, we can see that while C_σ for opaque cloud anomalies is the dominant term for δT_x, δT_m, and δT_n, B_σ for precipitation anomalies is the dominant term for δDTR, the δRH variables, as well as δP_{LCLtx} and δQ_{tx}. Comparing with equation (12), we see a reduction of the dependence on δOpaqueCloud$_\sigma$ and increased dependence on δPrecipWT$_\sigma$ for $\delta T_{x\sigma}$, δDTR$_\sigma$, δRH$_{tx\sigma}$, and $\delta P_{LCLtx\sigma}$ with this shift from monthly to seasonal averaging.

Figure 6 shows the dependence of δT_x on δOpaqueCloud, sorted by δPrecip (AMJJA), and δDTR, δRH$_{tx}$, and δP_{LCL} on δPrecip (AMJJA), sorted by δOpaqueCloud. The black data points are for $-0.5 < \delta X < 0.5$, red for $-1.5 < \delta X < -0.5$, and blue for $0.5 < \delta X < 1.5$, where X is the precipitation in mm/d or opaque cloud cover in tenths. The small number of points (total of 26) that are outside these ranges are not shown. The plotted lines with the same colors are the regression fits from Table 4, corresponding to the midpoints of the opaque cloud bins (-1, 0, and 1), which correspond to $\pm10\%$ change in cloud cover, and the midpoints of the precipitation bins (-1, 0, and 1 mm/d). Thus, red (blue) colors denote a growing season that has reduced (increased) mean precipitation and cloud cover. Figure 6 clearly show the codependency of four key climate
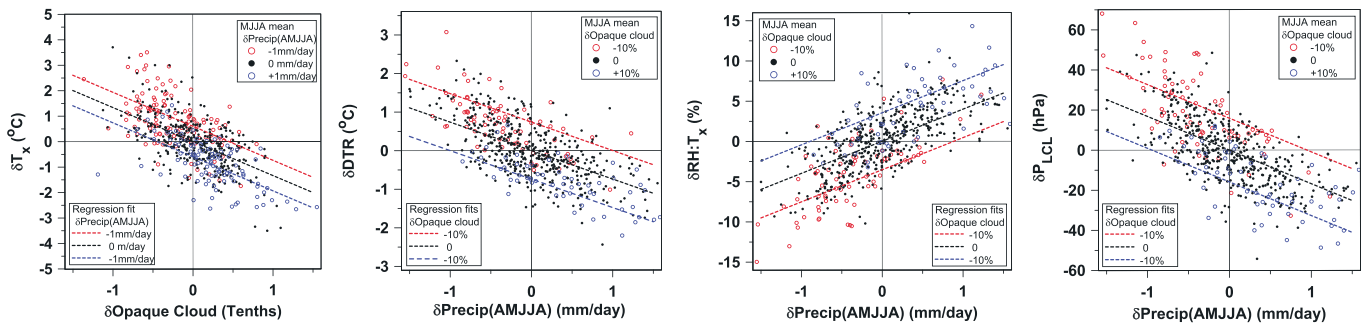
Figure 6. Dependence of δT_x on δOpaqueCloud sorted by δPrecip (AMJJA) and δDTR, δRH$_{tx}$, and δP_{LCLtx} on δPrecip (AMJJA) sorted by δOpaqueCloud.

variables (those with the highest R^2 values in Table 4) on the growing season precipitation and opaque cloud cover anomalies.

5.2. Coupling Between DTR, T_x, RH$_{tx}$, and P_{LCLtx}

For the regression analyses above, we have considered station precipitation and cloud as external variables influencing surface climate, even though the cloud field and precipitation also respond to surface as well as large-scale forcing in the fully coupled system. The internal coupling between the characteristics of the diurnal climate is also of interest, as shown in Figure 3 for the 11 station long-term mean. For the growing season climate, Figure 7 plots opaque cloud against precipitation, and T_x, RH$_{tx}$, and P_{LCLtx} against DTR, which is a key observable. Starting with the anomaly data, $\delta Y = \delta$OpaqueCloud, δPrecip, δT_x, δDTR, δRH$_{tx}$, and δP_{LCLtx}, we reconstructed Y by adding the MJJA average of the 582 growing season means (Y_{MJJAm}).

$$Y = Y_{MJJAm} + \delta Y$$

For these plots, we show the geometric mean slope, given using Deming regression with the (x, y) error ratio estimated as the ratio of the standard deviation of the variable pairs. The uncertainty estimates are approximated as half the 95% confidence limits. The relation between cloud cover and precipitation (Figure 7, left) has slope δOpaqueCloud = 0.73($\pm$0.13)*δPrecip, but the correlation is poor ($R^2 = 0.17$). For the plots of T_x, RH$_{tx}$, and P_{LCLtx} against DTR, the correlation is higher (with $R^2 = 0.51$ to 0.53).

Table 5 (left columns) gives the slopes for this set of 580 MJJA means, including also $\delta\Delta$RH. Note that the slope given by Deming regression is the ratio of the standard deviations for a variable pair. Table 5 (right columns) are the corresponding regression slopes calculated using the 2341 separate growing season months. The R^2 values increase, and the uncertainty estimates fall with the larger data sample size. Except for T_x, the mean slopes fall using monthly data, but these differences in slope between monthly and seasonal means are comparable to the error estimates. However, the smaller uncertainty of the monthly regression slopes may be more useful for comparing these observed relationships with those in models.

6. Coupling Growing Season Climate to Simplified Prairie Energy and Water Budgets

For the 11 stations, the mean MJJA precipitation is 1.94($\pm$0.08) mm/d, and the mean opaque cloud cover is 4.48($\pm$0.08) tenths (44.8%). Figure 6 and Tables 4 and 5 show the interdependence of temperature and humidity variables, precipitation, and opaque cloud anomalies. This observed climate coupling between near-surface variables, derived from nearly 600 station years of data in sections 3, 4, and 5 for the Canadian Prairies, is of value for evaluating large-scale models, where the surface, BL, and cloud processes are generally parameterized. From a conceptual viewpoint, it would also be helpful if these coupled observables could be linked to the components of a corresponding simplified energy and water budget for the Prairies in the growing season. For example, can we derive the linkage between DTR, RH$_{tx}$, and EF, as precipitation and cloud change? On climate time scales, we have two key components: the mean precipitation in the water budget; and we can estimate the surface R_n in the surface energy budget (equation (1)) from mean opaque cloud cover and the surface albedo (section 6.4). The critical missing component is the surface evaporation, for which we have no data on the scale of the Prairies. However, on these large spatial and temporal scales,
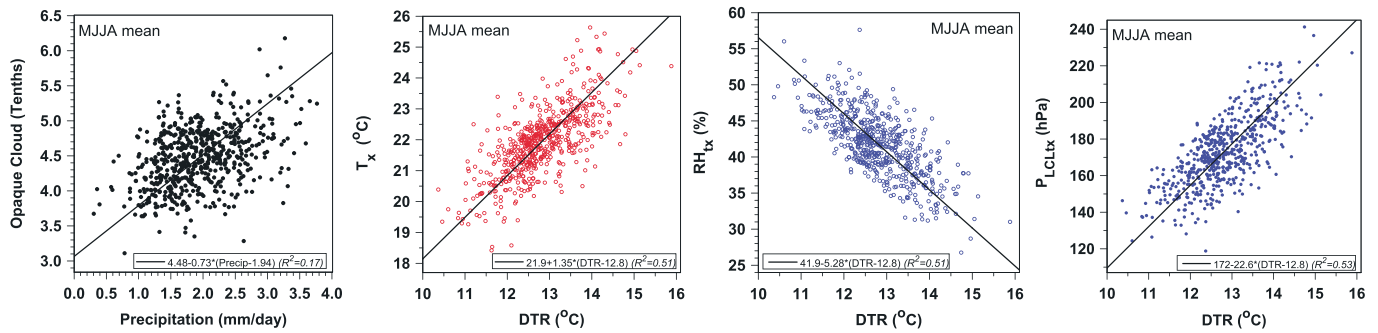
Figure 7. Coupling between opaque cloud and precipitation: T_x, RH_{tx}, and P_{LCLtx} and DTR for growing season means.

we can estimate the seasonal coupling between the drydown in total surface water storage and the seasonal anomalies of precipitation using the GRACE data.

The surface water balance for the growing season can be written as

$$\Delta TWS = P - E - R \tag{15}$$

where P, E, and R are, respectively, the precipitation, evapotranspiration, and runoff and ΔTWS is the change in the total water storage, which includes all the water reservoirs in the soil and on the landscape. Rearranging gives an estimate of E as

$$E = P - R - \Delta TWS. \tag{16}$$

Most of the runoff on the Prairies is associated with the melt of the snowpack in spring, and summer runoff is $<0.1\,P$ [*Sauchyn et al.*, 2009; *Wang et al.*, 2014a]. However, in the past few decades, the Prairie river basins have become heavily regulated to manage the winter and spring flows. Data from the S. Saskatchewan River will be used to make a rough estimate of R/P in recent decades in section 6.1.

Total water storage typically falls from a peak after snowmelt through the summer season, so ΔTWS is negative, and contributes to increased evapotranspiration. *Sauchyn et al.* [2009] estimate that the withdrawal of available soil moisture in the growing season is on the order of 100 mm, but it is likely that there is a dependence on precipitation anomalies, as well as changes in cropping over the decades [*Betts et al.*, 2013b]. Our data set has one possible observational indicator; the fall of opaque cloud cover from June to August seen in Figure 2 (top left) is reduced with increasing precipitation. This may reflect a reduced seasonal decline of soil water, because the coupling between clouds, soil water, and EF is seen in observations [*Gentine et al.*, 2013b] and in numerical simulations [*Betts and Viterbo*, 2005]. We will use the recent decade of gridded land data from GRACE to link the growing season drydown of total water storage (TWS) [*Yang et al.*, 2011; *Cai et al.*, 2014] to precipitation anomalies on large spatial scales (section 6.2).

6.1. Growing Season Runoff for S. Saskatchewan River

The S. Saskatchewan River drains much of the Prairies of Alberta and part of Saskatchewan. Monthly streamflow records and a gridded precipitation product exist for 1958–1996 [*Wang et al.*, 2014a, 2014b], so we used these data to assess the runoff ratio R/P for MJJA. Streamflow has declined with time, as the Prairie River systems have become managed to supply water to cities, agriculture, and mining [*Saskatchewan Water Security Agency*, 2014]. In 1967, the Gardiner and Qu'Appelle dams in Saskatchewan were completed that created Lake Diefenbaker, so that some of the flow on the S. Saskatchewan River could be diverted to the Qu'Appelle River that flows across southeastern Saskatchewan into Manitoba. As a result, MJJA R/P for the S. Saskatchewan River declined from $13.4 \pm 2.9\%$ for 1959–1967 before the dams were completed, to $7.0 \pm 4.4\%$ for 1968–1977, to $4.7 \pm 2.9\%$ for the most recent period of 1978–1996. Given these changes with time associated with the regulation of the river since 1967, we decided that it was not realistic to couple the runoff ratio to precipitation; so we set the runoff ratio for the MJJA Prairie water budget at a fixed approximate value of 5%, giving
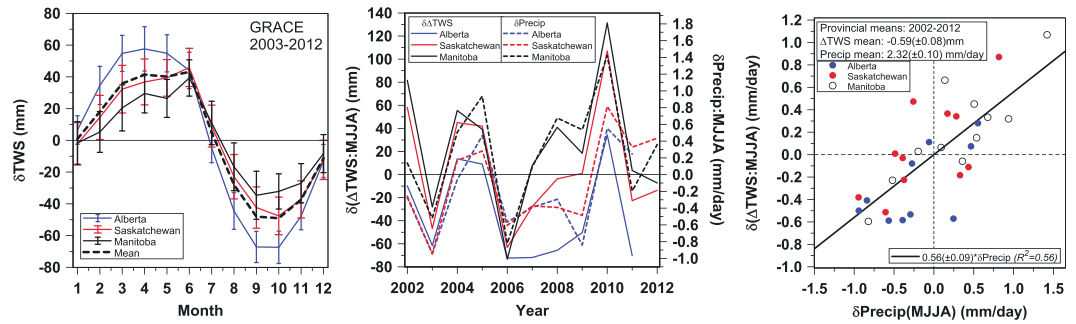
$$R/P = 0.05 \tag{17}$$

Figure 8. (left) Mean annual cycle of GRACE δTWS by province, (middle) interannual variability of mean growing season dry-down ΔTWS:MJJA and precipitation anomalies for each province, and (right) scatterplots with regression fit.

6.2. Coupling Growing Season ΔTWS to Precipitation Anomalies using GRACE Data

We will use the gridded $1 \times 1°$ monthly landmass grids [*Swenson and Wahr*, 2006; *Landerer and Swenson*, 2012], version JPL-RL05.DSTvSCS1401 dated 14 February 2014 (processed by the Jet Propulsion Laboratory), for liquid water equivalent thickness from the GRACE for 2002–2012 to estimate the growing season change of ΔTWS on large spatial scales. Then we will couple ΔTWS to precipitation anomalies for the growing season.

The GRACE data have been proven very useful for evaluating the interannual variability of the terrestrial water storage in models for global river basins [*Yang et al.*, 2011], the Mississippi basin [*Cai et al.*, 2014], and the Canadian river basins [*Lambert et al.*, 2013; *Wang et al.*, 2014a, 2014b], as well as climate extremes such as the 2003 European heat wave [*Andersen et al.*, 2005]. There is uncertainty in the long-term trends in the GRACE data, in part because of isostatic adjustment [*Lambert et al.*, 2013], so we removed the 2002–2012 trends, which are small in this data set (for Alberta, Saskatchewan, and Manitoba, they are 6.8 ± 1.6, 5.5 ± 1.5, and -2.0 ± 1.3 mm/yr, respectively). Their removal has very little impact on the growing season changes of ΔTWS. Although the data have been interpolated to a $1 \times 1°$ grid for user convenience, the effective spatial resolution of the GRACE data is about 300 km, because the processing involves considerable horizontal smoothing [*Swenson and Wahr*, 2006; *Landerer and Swenson*, 2012; *Wang et al.*, 2014a].

Figure 8 (left) shows the mean annual cycle of δTWS for the decade of 2003–2012, where δTWS is the perturbation from the decadal mean, for three provincial Prairie regions: Alberta is (49 to 54°N, -114 to $-110°$W); Saskatchewan is (49 to 53°N, -110 to $-102°$W); and Manitoba is (49 to 51°N, -101 to $-96°$W). The amplitude of the mean annual cycle decreases across the Prairies from 125 mm in Alberta, 87 mm in Saskatchewan, to 64 mm in Manitoba. There is a spring maximum in April after snowmelt in Alberta, but further east, the maximum is in June, the month of maximum precipitation. The fall minimum is in September or October. For each province, we estimated δTWS on 1 May as the mean of April and May, and on 31 August as the mean of August and September, and calculated anomalies of the drydown ΔTWS: MJJA from 1 May to 31 August. The mean value of the ΔTWS for the 10 year climatology in Figure 8 (left) is -79 mm.

The effective spatial resolution of the GRACE data of about 300 km means that a direct comparison with climate station monthly precipitation data is not possible, because there is a mismatch of scale. For example, the stations Moose Jaw and Regina are only 64 km apart, but their growing season precipitation differ widely in some years, since they are point measurements influenced by convective rainfall. However, their derived GRACE ΔTWS:MJJA barely differ, because they are in adjacent grid boxes. So we averaged over the three prairie regions given above and compare with the corresponding mean of the growing season precipitation from all the stations within each region for each year. For this, we used the monthly archive (http://ec.gc.ca/dccha-ahccd/) of the second generation adjusted precipitation data set [*Mekis and Vincent*, 2011], which was carefully reprocessed to preserve the long-term trends out to the century time scale, as instruments have changed. For the comparison with GRACE, we need only the recent data from 2002 to 2012. This data set has many more precipitation stations than the 11 climate stations in Table 1 (which have a full set of hourly variables including RH and opaque cloud). There are many more stations with data in the years 2002–2007 (19 in Alberta, 16 in Saskatchewan, and 11 in Manitoba), but by 2011, the corresponding numbers in this monthly archive are reduced to (4, 8, and 5). This second generation
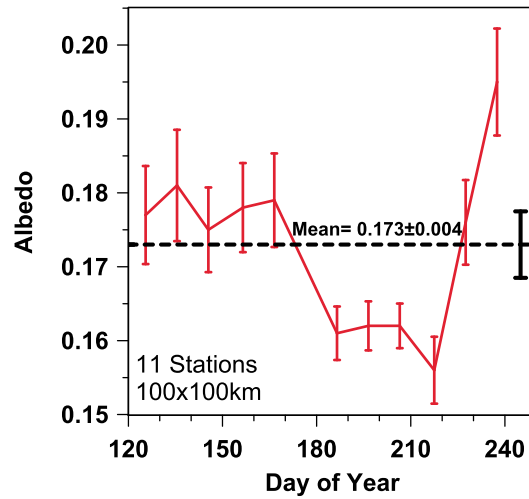
Figure 9. Mean seasonal cycle of albedo and MJJA mean for 100×100 km grid boxes enclosing the 11 Prairie stations.

precipitation has a number of corrections [*Mekis and Vincent*, 2011] that have increased monthly precipitation. For the recent decade of the 2000s, this increase is $5.5 \pm 0.2\%$ for MJJA, derived by comparing this second generation data with our monthly values coming from the original daily archive. For consistency with the rest of our analysis derived from the unadjusted daily data, we reduced these second generation precipitation data by 5.5%.

Figure 8 (middle) shows the interannual variability of the computed anomalies of ΔTWS: MJJA and precipitation for each province. Figure 8 (right) plots anomalies δ (ΔTWS:MJJA) against δPrecip (MJJA) for the years 2002–2012. We show all years, except for 2012 in Alberta, where there are only 2 stations with precipitation data. The linear regression fit with $R^2 = 0.56$ is

$$\Delta\text{TWS} : \text{MJJA} = -0.59(\pm 0.08) + 0.56(\pm 0.09)\ \delta\text{Precip(MJJA)} \tag{18}$$

So equation (18)b shows that as δPrecip (MJJA) decreases from $+1$ to -1 mm/d, ΔTWS:MJJA increases from near zero to -1.15 mm/d, which corresponds to -141 mm over the 123 day growing season. The coupling coefficient of $0.56(\pm 0.09)$ in equation (18) means that evapotranspiration anomalies from our simplified water budget (equation (16)) are heavily damped (see equation (20a) below).

There are several uncertainties in this analysis. We have mentioned the decline of precipitation data after 2007, but limiting the analysis to just 2002–2007 does not change our results within the uncertainty. There are substantial variations in soils and water storage across the Prairies, and Figure 8 (left) suggests that the TWS drydown has a west-east variation. However, the anomalies shown in Figure 8 (right) are as large in Manitoba as in Alberta. Other issues need further study. In Alberta, snow cover in the mountains may impact the GRACE footprint in spring, and in Manitoba, lake levels to the north of Winnipeg may impact the GRACE footprint. Clearly, a more extensive analysis may be justified, but we shall use equation (18) in a simplified water budget for the Prairies in the growing season.

6.3. Simplified Growing Season Water Budget

We will use equation (18) to represent the growing season drydown as

$$\Delta\text{TWS} : \text{MJJA} = \Delta\text{TWS}_m + F^*\ \delta\text{Precip(MJJA)} \tag{19}$$

where $\Delta\text{TWS}_m = -0.59$ mm/d, equivalent to a drydown of 73 mm for MJJA, and $F = 0.56$. These values were derived for the recent decade, but we will apply them to the much longer time series for the Prairies for which $P_m = 1.94$ mm/d. Inserting equations (17) and (19) into equation (16) gives an estimate of the growing season evapotranspiration of

$$E = 0.95(P_m + \delta\text{Precip(MJJA)}) - \Delta\text{TWS}_m - F\ \delta\text{Precip(MJJA)}$$

$$= 0.95 P_m - \Delta\text{TWS}_m + (0.95 - F)\ \delta\text{Precip(MJJA)} \tag{20a}$$

$$= 2.43(\pm 0.12) + 0.39(\pm 0.09)\ \delta\text{Precip(MJJA)} \tag{20b}$$

where we have neglected the uncertainty in the runoff ratio R/P, which was given the fixed value of 0.05. Note that $F > 0$ damps the role of precipitation anomalies on E.

This simplified water budget is only an approximate long-term mean for the Prairies. The GRACE data estimates of soil drydown are only from the recent decade. The runoff ratio has changed over time with increased river water management, and substantial shifts in parts of the Prairies from summerfallow to annual cropping over the past 30 years may have increased the extraction of root zone soil moisture by increased transpiration [*Sauchyn et al.*, 2009; *Betts et al.*, 2013b].
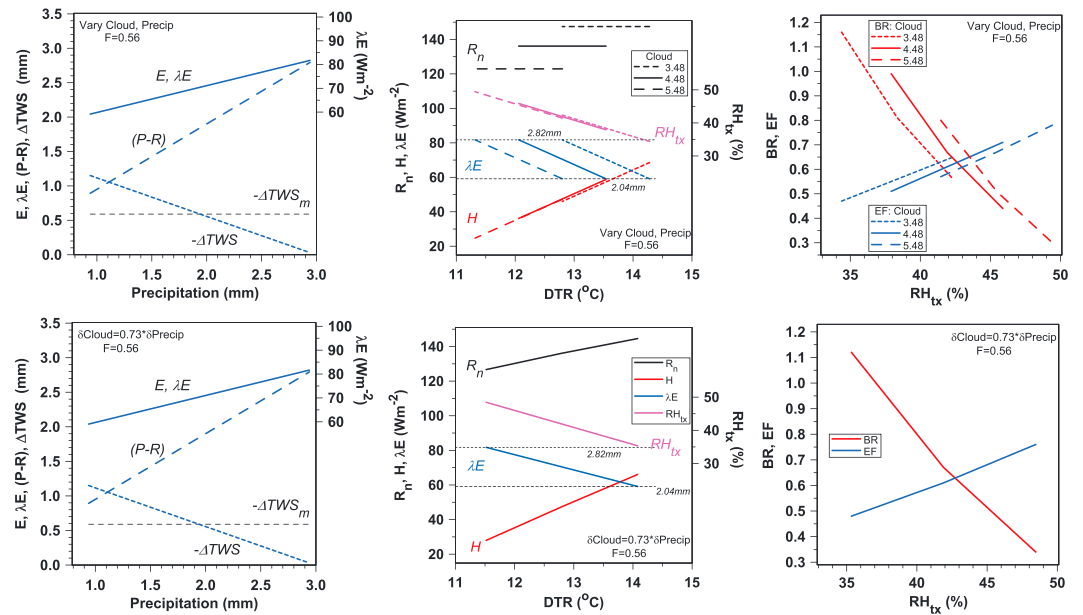
Figure 10. (left column) Moisture budget terms as a function of precipitation, (middle column) coupling of energy fluxes and RH_{tx} to DTR, and (right column) coupling of EF and BR to RH_{tx} for a (top) range of opaque cloud and with (bottom) cloud coupled to precipitation.

6.4. Surface Radiation Budget

The surface radiation budget can be estimated from opaque cloud cover. The surface net radiation, R_n, can be expanded in terms of the net shortwave and longwave fluxes, SW_n and LW_n, and their components, the upward and downward fluxes (suffixes: up and dn)

$$R_n = SW_n + LW_n = (SW_{dn} - SW_{up}) + (LW_{dn} - LW_{up}) \qquad (21)$$

Opaque clouds reduce the downward shortwave flux, SW_{dn}, below its clear-sky value, $SW_{dn}(clear)$. This is expressed as the surface shortwave cloud forcing, SWCF, defined negative as

$$SWCF = SW_{dn} - SW_{dn}(clear). \qquad (22)$$

Betts and Viterbo [2005] and *Betts* [2009] defined an effective cloud albedo, ECA, as

$$ECA = -SWCF/SW_{dn}(clear). \qquad (23)$$

This is a dimensionless measure of the fraction of $SW_{dn}(clear)$ that is reflected or absorbed by the cloud field per unit area of the surface. This removes the seasonal change in the clear-sky flux. This effective cloud albedo plays a similar role to the surface albedo (α_s) in the surface energy balance, since the net shortwave flux can be written as

$$SW_n = (1 - \alpha_s)(1 - ECA)SW_{dn}(clear) \qquad (24)$$

where

$$\alpha_s = SW_{up}/SW_{dn} \qquad (25)$$

We derived the seasonal dependence of α_s for the Prairies from the 2001 Moderate Resolution Imaging Spectroradiometer albedo data set produced by the Canada Centre for Remote Sensing [*Betts et al.*, 2014]. The native data are 250×250 m pixels with a 10 day frequency (late June 2001 is missing). These were averaged to 50×50 km grid boxes and then the four boxes enclosing each of the 11 Prairie stations in Table 1 were averaged.

Figure 9 shows the mean seasonal cycle for the 11 stations, with the standard error estimate and the MJJA mean of 0.173 ± 0.004. There is a drop in albedo from 0.178 in spring to 0.160 at the peak of the growing season and a rise at the end of August as crops are harvested.

Table 6. Solutions for Water and Energy Budget for $F = 0.56$ and δOpaqueCloud $= 0.73{*}\delta$Precip

Precipitation (mm/d)	Cloud (Tenths)	E (mm/d)	T_x (°C)	DTR (°C)	RH_x (%)	P_{LCLtx} (hPa)	$(R_n - G)$ (W/m^2)	H (W/m^2)	λE (W/m^2)	EF	BR
0.94	3.75	2.04	23.47	14.07	35.35	200.7	125.2	66.1	59.1	0.48	1.12
1.94	4.48	2.43	21.90	12.80	41.90	172.4	117.9	47.5	70.4	0.61	0.67
2.94	5.21	2.82	20.33	11.53	48.45	144.1	109.7	28.0	81.7	0.76	0.34
Δ: 2	1.46	0.78	−3.14	−2.54	13.10	56.6	−15.5	−38.1	22.6	0.28	−0.78

For SW$_{dn}$(clear), we will use fits derived in B13A as a function of latitude, from SW$_{dn}$ measurements at Lethbridge, Swift Current, The Pas, and Winnipeg, and data from the Boreal Ecosystem-Atmosphere Study and one of the Boreal Ecosystem Research and Monitoring Sites sites. This simplified fit, which has no dependence on aerosol or atmospheric water vapor, is

$$SW_{dn}(clear) = A + B{*}COS(\pi{*}(DOY - 170)/365))^2 \tag{26}$$

where the coefficients A and B are 63 and 322 at 50.76°N, the mean latitude of the 11 Prairie stations.

Betts et al. [2013a] derived a simplified fit between opaque cloud cover and ECA, which has no dependence on cloud height distribution or cloud structure, for the warm season period, May to August

$$ECA = 0.0681 + 0.0293\ OpaqueCloud + 0.00428\ OpaqueCloud^2 \tag{27}$$

Opaque clouds also increase the downwelling longwave flux, LW$_{dn}$, reducing the surface LW$_n$. B13A derived the warm season fit

$$LW_n = -100.1 + 4.73\ OpaqueCloud + 0.317\ OpaqueCloud^2 \tag{28}$$

Combining equations (21), (24), (25), (26), (27), and (28) gives R_n as a function of opaque cloud cover (in tenths) for MJJA.

6.5. Coupling of the Heat and Water Budgets and Near-Surface Climatology

We defined the surface energy balance in the introduction as

$$(R_n - G) = H + \lambda E \tag{29}$$

We have no observations for G, so will use the model data for the growing season from the European Centre Interim reanalysis for a Prairie grid point that includes Regina. For 1995–2012, this gives an estimate of $G = 0.134(\pm0.015)\ R_n$. Equation (20b) gives E in terms of precipitation, runoff, and the coupling parameter $F = 0.56$ estimated from the GRACE data. R_n is determined in terms of cloud cover in section 6.4. In equation (24), we used the seasonal dependence of α_s, and in equations (27) and (28), we included the monthly climatology of opaque cloud cover. Together, these give the surface fluxes, EF and BR, in terms of opaque cloud and precipitation and their anomalies. We now merge the water and energy budgets with the regression relations from Table 4, which relate temperature and humidity anomalies to opaque cloud and precipitation anomalies. Strictly, the precipitation anomalies in equations (13) and (14) included a contribution from April precipitation anomalies, since this slightly increased the explained variance. However, removing April and leaving only MJJA introduces a negligible change (<2%) in the regression coefficients on precipitation and opaque cloud anomalies.

Figure 10 shows the relations between some key variables. The top row is for ranges of δPrecip $= \pm1$ mm/d and δOpaqueCloud $= \pm1$ tenth about the long-term Prairie means, while the bottom row couples opaque cloud and precipitation using their growing season climate relation from Figure 7.

$$\delta OpaqueCloud = 0.73(\pm0.13){*}\delta Precip \tag{30}$$

The left column shows the components of the water and evaporation budgets. The panels are identical because there is no dependence on cloud. ΔTWS is nearly zero with $F = 0.56$ for the wet solution with Precip $= 2.94$ mm/d (δPrecip $= +1$ mm/d); that is with sufficient rain, there is no drydown of total water storage, as discussed in section 6.3. The right-hand scale shows λE.

The middle column shows the components of the surface energy balance as a function of DTR, which is derived as a function of precipitation and opaque cloud using the regression relation in Table 4. The slope of RH_{tx} with DTR has almost no dependence on cloud: this is the same relationship shown in Figure 7. R_n

depends only on surface albedo and opaque cloud (section 6.4), but the partition of R_n into the surface fluxes λE and H depend on both precipitation and cloud, because E varies with precipitation (Figure 10, left). In Figure 10 (top), these fluxes are plotted for the three ranges of opaque cloud, corresponding to δOpaqueCloud = −1, 0, and 1 tenths about the long-term Prairie mean; in Figure 10 (bottom), we use equation (30). For λE, we show the corresponding extremes of E from the left columns. Note that with $F = 0.56$, and the small range of E, the dependence of H on DTR collapses to nearly a single line for the three cloud covers. The right column shows the dependence of BR and EF on afternoon RH_{tx}. Replacing RH_{tx} with DTR gives a similar plot (not shown), since DTR and RH_{tx} are themselves tightly coupled (middle column).

Table 6 summarizes the coupling between the surface energy balance and the mean daily climate variables as shown in the bottomsetof Figure 10.

The mean precipitation of 1.94 mm/d and opaque cloud cover of 4.48 tenths give $(H, \lambda E) = (47.5, 70.4)$ W/m^2 and EF = 0.61. The bottom line is the difference between the solutions for δPrecip = ±1 mm/d. Note that $\Delta E < \Delta$Precip, because of the role of the coupling coefficient F in equation (20b). If we rescale in terms of a −1°C change in DTR, another observable, the corresponding climatological changes of OpaqueCloud, E, T_x, RH_x, P_{LCLtx}, $R_n - G$, H, λE, and EF are 0.57, 0.31, −1.24, 5.16, −22.3, −6.1, −15.0, 8.9, and 0.11, with the units given in Table 6.

Evapotranspiration from crops has a strong seasonal cycle [*Shrestha et al.*, 2012], while equation (20b) and Table 6 give a mean MJJA estimate from the large-scale water budget. For comparison, *Wang et al.* [2013] simulated 30 year (1979–2008) mean evapotranspiration for the entire Canadian landmass with a 1×1 km^2 spatial resolution, using the Ecological Assimilation of Land and Climate Observations model [*Fernandes et al.*, 2007] driven by remote sensing land surface data and gridded meteorological forcing. This bottom-up model integration shows the strong seasonal cycle of the Prairie ecozone, with an MJJA mean $E = 2.59$ mm/d, slightly larger than our estimate of 2.43(±0.12) mm/d. At the other extreme of point flux tower measurements, our E and R_n estimates are consistent with eddy covariance observations taken during the summer period of 2006, which gave a mean E of 2.34 mm/d with mean JJA precipitation of 1.91 mm/d, over an upland mixed grass site in the St. Denis National Wildlife Area, 40 km east of Saskatoon, Saskatchewan [*Armstrong et al.*, 2008].

Table 6 linking observables and our simplified energy and water budget for the growing season provides a useful conceptual framework for the climate sensitivity of the fully coupled land-surface-atmosphere system over the Prairies to precipitation and cloud anomalies. There are many uncertainties: the uncertainty in R_n based on the fits to opaque cloud is small [B13A], and the uncertainty in the growing season regression relations is shown in Table 4. These are based on the past 50 years, during which there have been substantial changes in cropping on the Prairies, which we have not considered here. The simplified water budget in section 6.3 applies the coupling coefficient F from Figure 8, based on a recent decade of GRACE data, to the long-term climate data.

7. Conclusions

The objective of this paper was to describe and understand how precipitation and cloud cover are linked to the warm season climatology of temperature and humidity, using the long-term data sets from 11 climate stations across the Canadian Prairies. Earlier work [B13A] showed that on daily time scales, there is a strong coupling between opaque cloud cover and T_x, DTR, RH_{tx}, and ΔRH. They showed that the DTR, a crucial observable, depends climatologically on opaque cloud cover on daily time scales, because cloud cover determines primarily T_x through the SWCF. They then calibrated opaque cloud cover against SWCF and net longwave to determine net radiation. Since we have for the first time estimates of the cloud radiative forcing for nearly 600 station years of data, we are able to quantify the distinct impacts of opaque cloud cover and precipitation on the surface climate using observations. On daily time scales, the primary diurnal climate dependence on cloud cover is little affected by daily precipitation.

At the other extreme, the 50 year climate time scale, we found that there is a tight coupling of summer temperature with opaque cloud and hence R_n. However, on this climate time scale, near-surface RH, P_{LCL}, and DTR are all tightly coupled to precipitation, not cloud cover; presumably because on long time scales, precipitation controls the water balance and specifically soil water. On monthly and seasonal time scales, however, anomalies of both opaque cloud cover and precipitation determine the anomalies of temperature and moisture.

On monthly time scales, we performed multiple linear regression between T and RH anomalies (and their diurnal ranges) against anomalies of opaque cloud for the current month and precipitation for the current and earlier months. Throughout the warm season from May to October, we found strong dependence on month-1 precipitation, and for MJJA, there was also additional weak dependence of RH anomalies on month-2 precipitation anomalies. We can interpret this longer growing season memory of precipitation anomalies as an indicator of crop rooting drawing on soil water from deeper layers. We show that anomalies of opaque cloud and precipitation explain a remarkable 60–80% of the variance in DTR, RH_{tx}, and LCL on monthly time scales. We then calculated a single set of regression coefficients for the growing season based on monthly data for MJJA, for which the explained variance is a little less.

We merged the months MJJA to a growing season mean, standardized the variables by dividing by their standard deviations, and again used multiple linear regression to couple anomalies of T_x, DTR, RH_{tx}, and P_{LCLtx} to anomalies of precipitation and cloud for the growing season. Comparing monthly to seasonal time scales, DTR, RH_{tx}, and P_{LCLtx} have more dependence on precipitation, presumably linked to soil water, and less dependence on opaque cloud. We showed, using both growing season MJJA means and the corresponding monthly means, how the internal characteristics of the diurnal climate (T_x, RH_{tx}, ΔRH, and P_{LCLtx}) are coupled to a key observable DTR. These observational relationships of the fully coupled system on monthly and seasonal time scales will be useful for evaluating the representation of the coupled processes in large-scale models.

We then derived the coupling between the growing season drydown of the GRACE-gridded land total water storage and MJJA precipitation anomalies and found that the seasonal drydown of TWS damps 56% of the MJJA precipitation anomalies. This relation enables us to estimate E in the simplified growing season water budget and then partition the surface energy budget into λE and H, using the relationship between opaque cloud cover and R_n. We estimated that the Prairie mean evaporative fraction is 0.61 and showed its dependence on precipitation and cloud anomalies. As a result, we could tabulate how growing season anomalies of precipitation and opaque cloud cover are coupled to both the surface fluxes of sensible and latent heat, as well as the surface diurnal climate, represented by the observables DTR, T_x, RH_{tx}, and P_{LCLtx}.

Observational relationships of the fully coupled system on monthly, seasonal, and climate time scales are essential, because we rely on well-validated global models for weather and seasonal forecasting and climate simulation. Modeling studies are also needed to link the surface evapotranspiration directly to the soil water budget, crop rooting, and phenology, which are not addressed here. Nonetheless, it is clear that the addition of the opaque cloud data, which give a climatological estimate of the SWCF and net longwave fluxes over the full range of time scales from diurnal to 50 years, gives new observational insight into the role of cloud forcing on the land-surface diurnal cycle across time scales.

References

Andersen, O. B., S. I. Seneviratne, J. Hinderer, and P. Viterbo (2005), GRACE-derived terrestrial water storage depletion associated with the 2003 European heat wave, *Geophys. Res. Lett.*, *32*, L18405, doi:10.1029/2005GL023574.

Armstrong, R. N., J. W. Pomeroy, and L. W. Martz (2008), Evaluation of three evaporation estimation methods in a Canadian prairie landscape, *Hydrol. Process.*, doi:10.1002/hyp.7054.

Beljaars, A. C. M., P. Viterbo, M. J. Miller, and A. K. Betts (1996), The anomalous rainfall over the United States during July 1993: Sensitivity to land surface parameterization and soil moisture anomalies, *Mon. Weather Rev.*, *124*, 362–383.

Betts, A. K., and P. Viterbo (2005), Land-surface, boundary layer and cloud-field coupling over the south-western Amazon in ERA-40, *J. Geophys. Res.*, *110*, D14108, doi:10.1029/2004JD005702.

Betts, A. K. (2000), Idealized model for equilibrium boundary layer over land, *J. Hydrometeorol.*, *1*, 507–523.

Betts, A. K. (2004), Understanding Hydrometeorology using global models, *Bull. Am. Meteorol. Soc.*, *85*, 1673–1688.

Betts, A. K. (2007), Coupling of water vapor convergence, clouds, precipitation, and land-surface processes, *J. Geophys. Res.*, *112*, D10108, doi:10.1029/2006JD008191.

Betts, A. K. (2009), Land-surface-atmosphere coupling in observations and models, *J. Adv. Model Earth Syst*, *1, Art. #4*, doi:10.3894/JAMES.2009.1.4. [Available at http://james.agu.org/index.php/JAMES/article/view/v1n4/JAMES.2009.1.4.]

Betts, A. K., and J. C. Chiu (2010), Idealized model for changes in equilibrium temperature, mixed layer depth and boundary layer cloud over land in a doubled CO_2 climate, *J. Geophys. Res.*, *115*, D19108, doi:10.1029/2009JD012888.

Betts, A. K., B. Helliker, and J. Berry (2004), Coupling between CO_2, water vapor, temperature and radon and their fluxes in an idealized equilibrium boundary layer over land, *J. Geophys. Res.*, *109*, D18103, doi:10.1029/2003JD004420.

Betts, A. K., R. Desjardins, and D. Worth (2013a), Cloud radiative forcing of the diurnal cycle climate of the Canadian Prairies, *J. Geophys. Res. Atmos.*, *118*, 8935–8953, doi:10.1002/jgrd.50593.

Betts, A. K., R. Desjardins, D. Worth, and D. Cerkowniak (2013b), Impact of land use change on the diurnal cycle climate of the Canadian Prairies, *J. Geophys. Res. Atmos.*, *118*, 11,996–12,011, doi:10.1002/2013JD020717.

Betts, A. K., R. Desjardins, D. Worth, S. Wang, and J. Li (2014), Coupling of winter climate transitions to snow and clouds over the Prairies, *J. Geophys. Res. Atmos.*, *119*, 1118–1139, doi:10.1002/2013JD021168.

Cai, X., Z.-L. Yang, C. H. David, G.-Y. Niu, and M. Rodell (2014), Hydrological evaluation of the Noah-MP land surface model for the Mississippi River Basin, *J. Geophys. Res. Atmos.*, *119*, 23–38, doi:10.1002/2013JD020792.

Dickinson, R. E. (2000), How coupling of the atmosphere to ocean and land helps determine the timescales of interannual variability of climate. *J. Geophys. Res., 105*, 20,115–20,119.

Dirmeyer, P. A. (2000), Using a global soil wetness dataset to improve seasonal climate simulation, *J. Clim.*, *13*, 2900–2922.

Eltahir, E. A. B. (1998), A soil moisture–rainfall feedback mechanism 1. Theory and observations, *Water Resour. Res.*, *34*, 765–776.

Ferguson, C. R., and E. F. Wood (2011), Observed land–atmosphere coupling from satellite remote sensing and reanalysis, *J. Hydrometeorol*, *12*, 1221–1254, doi:10.1175/2011JHM1380.1.

Ferguson, C. R., E. F. Wood, and R. K. Vinukollu (2012), A global intercomparison of modeled and observed land–atmosphere coupling, *J. Hydrometeorol*, *13*, 749–784, doi:10.1175/JHM-D-11-0119.1.

Fernandes, R., V. Korolevych, and S. Wang (2007), Trends in land evapotranspiration over Canada for the period 1960–2000 based on in situ climate observations and a land surface model, *J. Hydrometeorol.*, *8*, 1016–1030, doi:10.1175/JHM619.1.

Findell, K. L., and E. A. B. Eltahir (1997), An analysis of the soil moisture–rainfall feedback, based on direct observations from Illinois, *Water Resour. Res.*, *33*, 725–735.

Findell, K. L., and E. A. B. Eltahir (2003), Atmospheric controls on soil moisture– Boundary layer interactions. Part I: Framework development, *J. Hydrometeorol.*, *4*, 552–569.

Findell, K. L., P. Gentine, B. R. Lintner, and C. Kerr (2011), Probability of afternoon precipitation in eastern United States and Mexico enhanced by high evaporation, *Nat. Geosci.*, *4*, 434–439, doi:10.1038/NGEO1174.

Gentine, P., A. Holtslag, F. D'Andrea, and M. Ek (2013a), Surface and atmospheric controls on the onset of moist convection over land, *J. Hydrometeorol*, *14*, 1443–1462, doi:10.1175/JHM-D-12-0137.1.

Gentine, P., C. R. Ferguson, and A. A. M. Holtslag (2013b), Diagnosing evaporative fraction over land from boundary-layer clouds, *J. Geophys. Res. Atmos.*, *118*, 8185–8196, doi:10.1002/jgrd.50416.

Hohenegger, C., P. Brockhaus, C. S. Bretherton, and C. Schär (2009), The soil moisture–Precipitation feedback in simulations with explicit and parameterized convection, *J. Clim.*, *22*, 5003–5020, doi:10.1175/2009JCLI2604.1.

Koster, R. D., and M. J. Suarez (2001), Soil moisture memory in climate models, *J. Hydrometeorol.*, *2*, 558–570.

Lambert, A., J. Huang, G. van der Kamp, J. Henton, S. Mazzotti, T. S. James, N. Courtier, and A. G. Barr (2013), Measuring water accumulation rates using GRACE data in areas experiencing glacial isostatic adjustment: The Nelson river basin, *Geophys. Res Lett.*, *40*, 6118–6122, doi:10.1002/2013GL057973.

Landerer, F. W., and S. C. Swenson (2012), Accuracy of scaled GRACE terrestrial water storage estimates, *Water Resour. Res.*, *48*, W04531, doi:10.1029/2011WR011453.

Lintner, B. J., P. Gentine, K. L. Findel, F. D'Andrea, A. H. Sobel, and G. D. Salvucci (2013), An idealized prototype for large-scale land-atmosphere coupling, *J. Clim.*, *26*, 2379–2389, doi:10.1175/JCLI-D-11-00561.1.

MANOBS (2013), Environment Canada MANOBS, Chapter 1, Sky. [Available at http://www.ec.gc.ca/manobs/default.asp?lang=En&n=A1B2F73E-1.]

Mekis, É., and L. A. Vincent (2011), An overview of the second generation adjusted daily precipitation dataset for trend analysis in Canada, *Atmos. Ocean*, *49*(2), 163–177.

Pal, J. S., and E. A. B. Eltahir (2001), Pathways relating soil moisture conditions to future summer rainfall within a model of the land–atmosphere system, *J. Clim.*, *14*, 1227–1242.

Saskatchewan Water Security Agency (2014), South Saskatchewan River project. [Available at https://www.wsask.ca/Lakes-and-Rivers/Dams-and-Reservoirs/Major-Dams-and-Reservoirs/South-Saskatchewan–River-Project-/.]

Sauchyn, D., E. Barrow, X. Fang, N. Henderson, M. Johnston, J. Pomeroy, J. Thorpe, E. Wheaton, and B. Williams (2009), Saskatchewan's natural capital in a changing climate: An assessment of impacts and adaptation. Report to saskatchewan ministry of environment from the prairie Adaptation Research Collaborative, 162 pp.

Schär, C., D. Lüthi, U. Beyerle, and E. Heise (1999), The soil–precipitation feedback: A process study with a regional climate model, *J. Clim.*, *12*, 722–741.

Seneviratne, S. I., D. Lüthi, M. Litschi, and C. Schär (2006), Land–atmosphere coupling and climate change in Europe, *Nature*, *443*, 205–209.

Shrestha, B. H., R. L. Raddatz, R. L. Desjardins, and D. E. Worth (2012), Continuous cropping and moist deep convection on the Canadian Prairies, *Atmosphere*, *3*, 573–590, doi:10.3390/atmos3040573.

Swenson, S. C., and J. Wahr (2006), Post-processing removal of correlated errors in GRACE data, *Geophys. Res. Lett.*, *33*, L08402, doi:10.1029/2005GL025285.

Wang, S., Y. Yang, Y. Luo, and A. Rivera (2013), Spatial and seasonal variations in evapotranspiration over Canada's landmass. *Hydrol. Earth Syst. Sci.,* *17*, 3561–3575, doi:10.5194/hess-17-3561-2013. [Available at http://www.hydrol-earth-syst-sci.net/17/3561/2013/.]

Wang, S., J. Huang, J. Li, A. Rivera, D. W. McKenney, and J. Sheffield (2014a), Assessment of water budget for sixteen large drainage basins in Canada, *J. Hydrol.*, *512*, 1–15.

Wang, S., D. W. McKenney, J. Shang, and J. Li (2014b), An assessment of long-term water budget closures for large drainage basins in Canada, *J. Geophys. Res. Atmos.*, *119*, 8712–8725, doi:10.1002/2014JD021951.

Yang, Z.-L., et al. (2011), The community Noah land surface model with multiparameterization options (Noah-MP): 2. Evaluation over global river basins, *J. Geophys. Res.*, *116*, D12110, doi:10.1029/2010JD015140.